UNIVERSITY OF COPENHAGEN
FACULTY OF SCIENCE

NIELS BOHR INSTITUTE

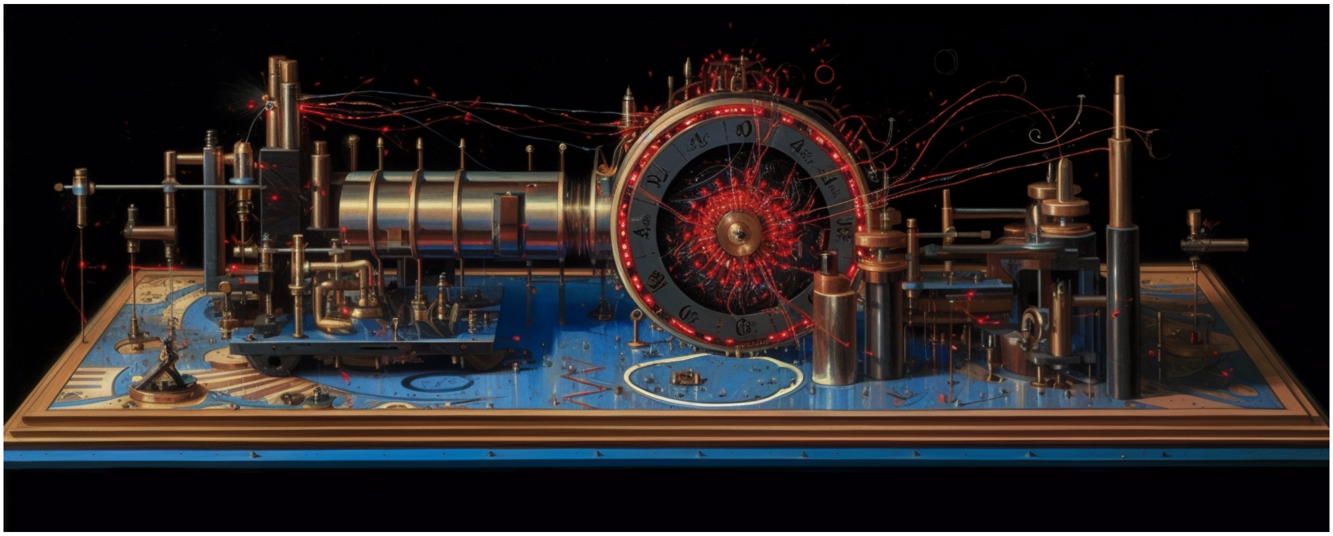

Master Thesis

Jonathan Guldberg Elsborg

Towards Continuous NICE-OHMS

an atomic beam machine

Date: 22.05.2023

Supervisors: Jörg Helge Müller, Asbjørn Arvad Jørgensen

Institute:	Niels Bohr Institute
Department:	Quantum Metrology
Author:	Jonathan Guldberg Elsborg
Title:	Towards Continuous NICE-OHMS, an atomic beam machine
Supervisors:	Jörg Helge Müller, Asbjørn Arvad Jørgensen
Date:	22.05.2023

Abstract

State of the art atomic clocks operate in discrete intervals, where atoms are captured and cooled, then released for spectroscopic measurements. This method imposes limitations in the form of long averaging times and aliasing of high frequency local oscillator noise, stemming from the time between measurements where the local oscillator has no reference. Continuous atomic clocks propose to avoid these limitations by separating atoms from the cooling lasers in space, rather than in time, allowing a beam of cold atoms to continuously pass through a spectroscopic measurement setup. This work presents a number of steps taken to realize such a continuous strontium beam machine. We explore the continuous deflection of a cold atomic beam and control the deflection using an electromagnetic bias field. The atomic beam is characterized in terms of atomic flux and temperature. A continuous atomic clock also imposes strict frequency stability requirements on any laser used in interactions with the atomic beam. An implementation of squash locking is made to explore prospects for long term stability for optically seeded diode lasers.

Resumé

Moderne atomure opererer i diskrete intervaller, hvor atomer bliver fanget og nedkølet, og derefter frigivet til spektroskopiske målinger. Denne metode gør det nødvendigt at midle målinger over mange timer og medfører aliasing af højfrekvent støj, som stammer fra tiden mellem målinger, hvor den lokale oscillator ikke har nogen reference. Kontinuerlige atomure kan potentielt undgå disse begrænsninger ved at rummeligt adskille atomerne fra kølelaserne, i stedet for at adskille dem i tid, hvilket tillader en stråle af kolde atomer at passere kontinuerligt gennem en spektroskopisk måleopstilling. Denne opgave præsenterer en række skridt imod realiseringen af en sådan kontinuerlig strontiumstrålemaskine. Vi udforsker den kontinuerlige afbøjning af en kold atomstråle og styrer afbøjningen ved hjælp af et elektromagnetisk felt. Atomstrålen karakteriseres i form af atomar flux og temperatur. Et kontinuerligt atomur stiller også strenge krav til frekvensstabilitet for enhver laser, der anvendes i interaktioner med atomstrålen. En implementering af squash locking foretages for at undersøge muligheder for langtidsstabilitet for optisk injicerede diodelasere.

Acknowledgments

I would like to thank my supervisor, Prof. Jörg Helge Müller, for his help and patience, and his willingness to talk physics at any time. And to my co-supervisor, Asbjørn Arvad Jørgensen, who is sadly not with us anymore (he got a better job). His help was invaluable, and his kindness kept me motivated. Many thanks to everyone in the Quantum Metrology group, Sofus, Eliot, Camila, Andrea, Mikkel and Stefan. They have all been more than generous in answering my questions and helping me grasp what is going on, as well as provide excellent company. A special thanks, with tea and biscuits, to Julian Robinson-Tait who is my supervisor in all but name. He gracefully took me under his wing and taught me most of what I know about atomic clocks. Any mistakes contained in this thesis are entirely his fault.

Thank you to all my friends at uni. You carried me through the tough times and made them great.

More than anything, thank you, Laura. For all your love and your amazing support. And for keeping the kids alive for the last month or so.

Contents

1 Introduction

The first atomic clock, finished in 1948, had an actual 12-hour clock face, with hands for hours, minutes and seconds, mostly to communicate the fact that the machine was a clock. Such visual pretense has since been abandoned, and the vacuum chambers of today, surrounded by lasers and electronics, do not visually give away their purpose. But they still seek to solve the same fundamental problem, counting time with ever greater precision. Atomic clocks make use of the fundamental properties of atoms. The well known discrete energy levels in atoms can be interrogated using lasers. Several different methods allow for stabilization of the laser to the frequency associated with the atomic transition, in effect turning the laser into a time keeping local oscillator. Knowing the energy of the atomic transition, Planck's law gives the frequency of the photon from $E = h\nu$. With frequency and time being inversely proportional, the oscillations of the laser become the ticking of time.

Today, advances in precision of time measurements are crucial in many fields of science and technology. Most famously, GPS satellites contains atomic clocks and the position measurements they enable are limited by the precision of their clocks. Current GPS devices allow for measurements of continental plate tectonics with movement speeds on the order of millimeters per year[1]. Changes in time due to gravitational time dilation has also been demonstrated as a method to measure altitude. With recent results resolving height differences on millimeter scale[2]. Very-long-baseline interferometry as used in the Event Horizon Telescope is only possible because measurements taken across the globe can be located in time with nanosecond precision[3].

Continuous atomic clocks is a current research field in atomic clocks. Several groups are pursuing methods of transforming their atomic clock experiments from discrete measurements into continuous atomic clocks. Contemporary discrete systems run on experimental cycles, where atoms are cooled and trapped. Then the trap is turned off to allow unperturbed frequency measurements on the atoms. With one such cycle typically taking a second or more. The continuous system has the benefit of avoiding the Fourier limit, and averaging out noise faster than in a discrete system. It also eliminates the frequency instability associated with the time between measurements in a discrete system. This instability is known as the Dick effect. Previous techniques used to eliminate the Dick effect involved the simultaneous operation of two atomic clocks[4], resulting in increased complexity.

This thesis represents parts of the effort to realize a continuous Strontium based clock, utilizing highly sensitive atomic interrogation techniques. Chapter 2 describes the relevant theory necessary to understand, how atoms can arrive continuously in an optical cavity. It also describes a common laser frequency stabilization scheme called injection locking, as well as a recent addition to that method, called squash locking. Finally, it gives an introduction to Noise Immune Cavity Enhanced Optical Heterodyne Molecular Spectroscopy (NICE-OHMS). A very sensitive spectroscopy technique that is expected to work well in the continuous regime. Chapter 3 describes the overall experimental setup. Subsection 3.3 describes the experimental setup for cooling and deflecting the continuous atomic beam. Is also describes the experimental results from tuning the atomic deflection and discusses these results. Subsection 3.4 describes the exploratory implementation of squash locking and describes the results thereof. It also discusses these results. Subsection 3.5 gives a brief description of a Python script that was written to facilitate real time analysis of atomic fluorescence. Chapter 4 summarizes the main results of the thesis and discusses future prospects of the work contained herein.

2 Theory

The following chapter gives a brief overview of the theoretical background necessary to understand the basics of the entire experimental setup, as well as some details specific to the experimental work done by the author.

2.1 Strontium 88

Our experiment uses ^{88}Sr atoms. The energy levels that are relevant for our experiment can be seen in fig 1. The $^1P_1 \rightarrow {}^1S_0$ transition has a relatively broad linewidth and fast decay rate at $\gamma/2\pi = 32MHz$. This makes it well suited for rapid laser cooling, since any excitation will rapidly decay through spontaneous emission. Thus keeping the transition available for further cooling. The large linewidth also means that interaction with the atoms are possible when there is a wider velocity distribution in the atomic beam. The $^3P_1 \rightarrow^1 S_0$ transition on the other hand has a narrow linewidth, making it well suited for μK cooling, as well as exploratory precision spectroscopy. In our case, it is used as a frequency reference. The $^3S_1 \leftrightarrow {}^3P_0$ and $^3S_1 \leftrightarrow {}^3P_2$ repumper transitions will be part of future work. Atoms decaying from $^1P_1 \rightarrow {}^1D_2 \rightarrow {}^3P_2$ will be unavailable for cooling as the $^3P_2$ has a slow decay rate. Over many cycles of absorption and spontaneous emission, this can lead to a significant number of atoms being shelved, unavailable for cooling and spectroscopy. The experimental setup as a whole is part of an exploratory study into continuous

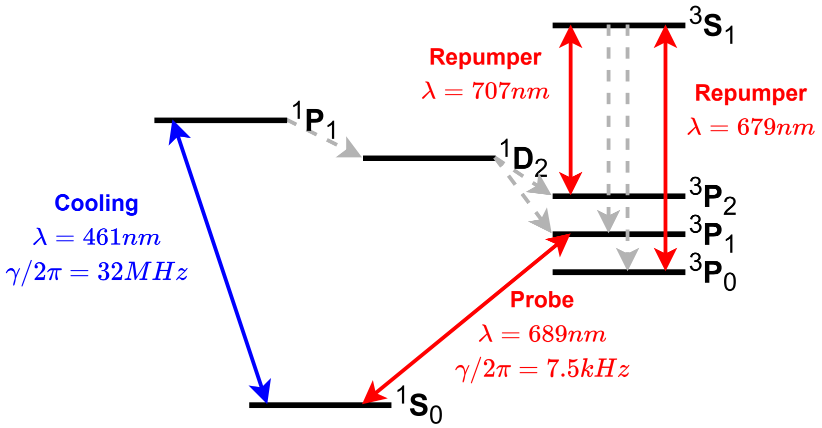

Figure 1: Relevant energy levels for ^{88}Sr atoms. Transitions driven by lasers are denoted with solid colored arrows. Spontaneous decay transitions are denoted with dashed gray arrows.

atomic beam clocks. Sr88 is well suited for this purpose because it is the most abundant isotope. It is also relatively easy to work with, with both fast and narrow transitions available. Sr88 has an energy level structure that closely resembles Sr87. Meaning that many of the techniques developed will be transferable to Sr87. And Sr87 has an ultra narrow $^3P_0 \leftrightarrow {}^1S_0$ transition with a linewidth on the order of $1mHz$ that can reach state-of-the-art clock precision[5]. This transition is available due to effects from nuclear spin. But working with the larger number of levels also adds complexity. Making ^{88}Sr well suited for exploratory studies.

2.2 Laser cooling and deflection

This is a brief explanation of the laser cooling techniques used in the experiment. The techniques are all well established and have been experimentally demonstrated in the late 80's[6–8]. As such, they are only briefly outlined to prepare the reader for the experimental results that use these cooling techniques.

The interaction between light and atoms makes it possible to change the velocity of the atoms. A photon that is on resonance with a transition in an atom can be absorbed, and the atom will now be in an excited state. When the photon is absorbed, the momentum of the photon is added to the momentum of the atom. So if the atom was travelling in the opposite direction of the photon, the atom will slow down a little. Through spontaneous emission, the atom will emit a photon again. But this photon will be emitted in a random direction, giving net-zero momentum change over many emissions. So over many such cycles of absorption and spontaneous emission, the atoms will on average be slowed down. The limiting factor here is the emission rate, or scattering rate. In a steady state system, the scattering rate is simply given as:

$$\gamma_p = \gamma\rho_{ee} = \frac{\gamma}{2}\frac{s_0}{1 + s_0 + (2\delta/\gamma)^2}, \tag{1}$$

$$s_0 = I/I_{sat}, \tag{2}$$

with γ_p being the scattering rate, γ the decay rate of the transition, ρ_{ee} the population in the excited state. $\delta = \omega_l - \omega_a$ is the detuning of the laser from the atomic transition. s_0 is the on-resonance saturation parameter [9]. For high saturation,

$s_0 >> 1$, the scattering rate simplifies to:

$$\gamma_p = \gamma/2 \tag{3}$$

The force on an atom in the process of continuous absorption and emission can then be described simply by the momentum of a photon, with energy equal to the transition, times the scattering rate:

$$F_{\mathtt{sp}} = \frac{\gamma}{2}\frac{\hbar k s_0}{1 + s_0 + (2\delta/\gamma)^2}, \tag{4}$$

Where $\hbar$ is the reduced Planck's constant and k is the angular wavenumber. This saturates to :

$$F_{\mathtt{sp}} = \hbar k \gamma/2, \tag{5}$$

When the atoms are moving, they experience a Doppler shift according to:

$$\omega_D = \omega_0 \left(\frac{v}{c}\right), \tag{6}$$

assuming non-relativistic velocities $v << c$. With ω_0 being the frequency of the transition in the rest frame, v being the velocity of the atoms along the axis of propagation for the laser, and c being the speed of light. When $\omega_D = -\delta$ the laser is on resonance with the atoms and the atoms will be slowed down by the continuous process of absorption and spontaneous emission. The atomic transition also has some linewidth, meaning a range of velocities interact with the laser. This is included if we now expand eq. (4) to include Doppler shift:

$$F_{\mathtt{sp}} = \frac{\gamma}{2}\frac{\hbar k s_0}{1 + s_0 + \left(2\left(\delta + \omega_D\right)/\gamma\right)^2}, \tag{7}$$

we obtain a Lorentzian function like in eq. (4), only now centered at $\delta = -\omega_D$, rather than at $\delta = 0$. At high saturation, the force approaches:

$$F_{\mathtt{max}} = \frac{\gamma \hbar k}{2}, \tag{8}$$

in turn, resulting in a maximum acceleration of:

$$a_{\texttt{max}} = \frac{\gamma \hbar k}{2M}, \tag{9}$$

where M is the atomic mass in kg. Using the blue transition in ^{88}Sr, this results in a maximum acceleration of $1.5 \cdot 10^5 m/s^2$ along the propagation direction of the laser. Instead of describing velocities, it can sometimes be helpful to describe the atomic cloud in terms of temperature. With the temperature given as:

$$T = \frac{v_{\text{rms}}^2 M}{k_B}, \tag{10}$$

this however, is not in strict accordance with the statistical framework of thermodynamics. Since the velocities of laser cooled atoms do not follow a Maxwell-Boltzmann distribution. Parts of the velocity distribution that have interacted with laser cooling may be compressed or otherwise changed. Despite this caveat, it can still be a useful parameter.

2.2.1 Optical molasses

Optical molasses is perhaps one of the simplest method of laser cooling atoms. The term is derived from the fact that the method slows the atoms down, as if they were moving through molasses. Here, we are mostly interested in counter-propagating laser beams. Usually achieved by retro-reflecting the same laser beam. The laser is detuned below the frequency of the atomic transition used for cooling. The force from the two beams then add up to:

$$F_{\pm} = \pm \frac{\gamma}{2} \frac{\hbar k s_0}{1 + s_0 + \left(2\left(\delta \mp |\omega_D|\right)/\gamma\right)^2}, \tag{11}$$

with the force given in scalar form, working along the laser beam propagation axis[9]. The force from each laser beam, F_+ and F_-, and their sum, is plotted in fig. 2.

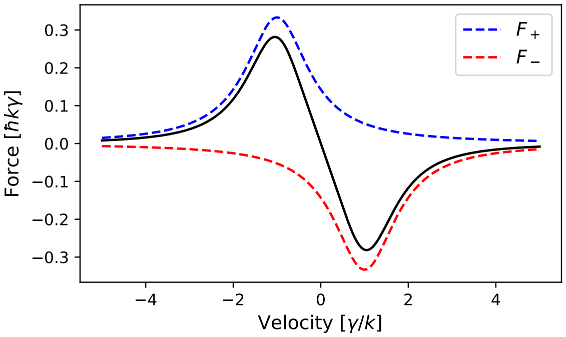

Figure 2: Total force on atoms in optical molasses, plotted in black, with $\delta = -\gamma$ and $s_0 = 2$. Force from each beam plotted in blue and red.

This shows that any atom, moving with relatively low velocity along the propagation axis of the laser beams, is met with a force in the opposite direction of the direction of motion. Higher velocities experience a greater Doppler shift and interact less with the laser. So only a finite range of velocities can be cooled using this method.

2.2.2 Zeeman splitting

Zeeman splitting is the phenomenon of atomic energy levels being split in the presence of an external magnetic field. Meaning that tuning of an external magnetic field allows for manipulation of atomic resonances. It is used in the cooling techniques outlined in section 2.2.3 and section 2.2.4. For this reason, it is explained here. Any atomic level that has non-zero angular momentum, $\vec{J} \neq 0$:

$$\vec{J} = \vec{L} + \vec{S} \tag{12}$$

will be split into $2J + 1$ sublevels[10]. Each with a shift in energy according to:

$$\Delta E = U(m_J) = \mu_B g_J m_J B, \tag{13}$$

where μ_B is the Bohr magneton, g_J is the Landé g-factor, m_J is the magnetic quantum number and B is the external magnetic field. Here, we will not worry about what is inside the Landé g-factor. Instead, we will simply use that it is equal to one for the ${}^1P_1$ state. Which reduces the energy shift of the m_J levels to:

$$\Delta E = \pm \mu_B B, \tag{14}$$

The resulting split is then on the order of $1.4MHz/G$ for the blue transition in ${}^{88}Sr$.

2.2.3 Zeeman slower

This section describes a method for slowing down a fast atomic beam. The force from radiation pressure from a single laser beam, given in eq. (7), only applies a force in a limited range of velocities. This presents a problem when our source of atoms provides high velocity atoms and a wide range of velocities. Meaning, no single value of δ will result in sufficient slowing of the atoms, since cooling will change the value of the Doppler shift, and bring the atoms away from resonance with the laser. To correct for this, a Zeeman slower uses a spatially varying magnetic field. This means that the Zeeman splitting of the atoms changes along the direction of travel of the atomic beam. Meaning, that with a careful choice of detuning and magnetic field, a wide range of velocities will interact with the laser and slow down[9]. As the atoms enter the Zeeman slower, the Zeeman shift is strong and fast atoms are slowed down. As they progress through the Zeeman slower, the magnetic field changes to ensure that as the atoms slow down and experience a smaller Doppler shift, the Zeeman splitting also decreases to keep the atoms on resonance with the laser. The laser has to be circularly polarized with the correct direction, to address the split energy level. Fig. 3 shows a schematic of an atomic beam, moving through a spatially varying magnetic field. The change in magnetic field is achieved by changing the number of coil windings along the path. And then changing the direction of current in the coils at the half-way point. Often in practice simply changing the direction of windings.

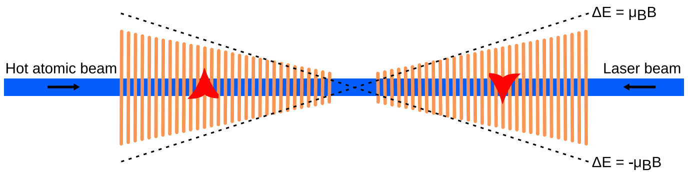

Figure 3: Schematic of a Zeeman slower. Orange lines denote tapering electromagnetic coils, resulting in tapering magnetic field strength. Red arrows denote current direction in coils. Energy level offsets, in dashed lines, depend on position, ensuring continuous interaction between atomic beam and laser beam along the entire Zeeman slower.

Typical velocity ranges that are captured in our system are in the range of $300 m/s$ or below and these are slowed down to a range of $50 m/s$ or below. The oven is typically run at $500°C$, resulting in a rms velocity of $v_{\text{rms}} = 530 m/s$, so many of the atoms are not interacting with the Zeeman slower and are not slowed down.

2.2.4 2D Magneto-Optical Trap

This section describes how a Magneto-Optical Trap (MOT) works. It is most widely used in a 3D configuration, with 3 laser beams, all retro-reflected, to ensure trapping and cooling of neutral atoms[9]. For simplicity, we will begin by explaining the 1D case and expand from there. A MOT utilizes a spatially dependent magnetic field to induce a spatially dependent energy shift on the atomic transition, like in the Zeeman slower. To achieve this field, electromagnetic coils are set up in an anti-Helmholtz configuration, like in fig. 4.

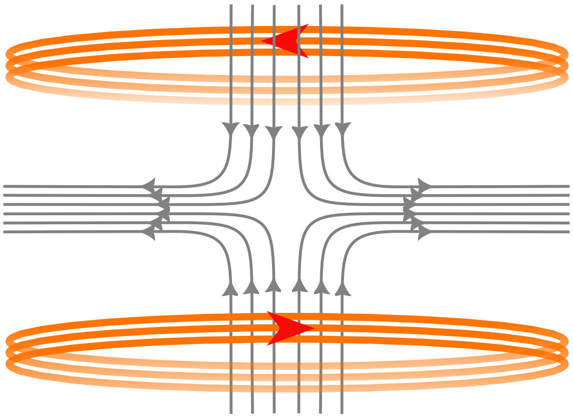

Figure 4: Magnetic field between two electromagnetic coils, arranged in an anti-Helmholtz configuration.

This configuration results in a magnetic field that is zero at the center point between the coil pair, and constant magnetic field gradients close to the center[11]. The resulting energy shifts are illustrated in fig. 5.

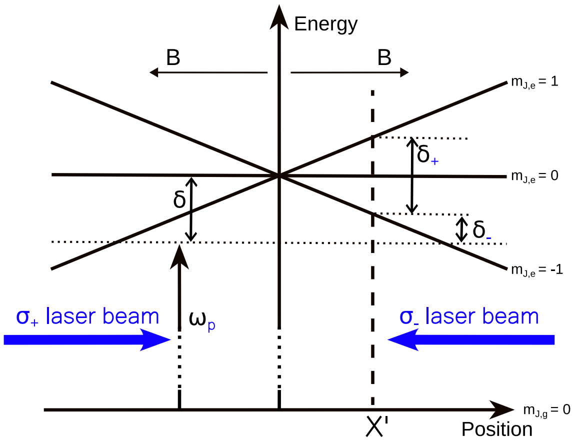

Figure 5: Fig. copied from [9], page 157. Schematic of position dependent energy shift in an atomic energy level with $J = 1$. The magnetic field increases linearly away from the center. Two circularly polarized laser beams, with opposite polarization direction, are incident from either side. The laser beams are detuned δ from the unperturbed $m_{J,e} = 0$ level. An atom at position x' is detuned δ_- from the σ_- laser beam, and detuned δ_- from the σ_+ laser beam.

With the correct choice of circular polarization direction and magnetic field sign, this configuration results in a position dependent force. The σ_+ laser beam addresses the $m_{J,e} = +1$ level, and the σ_- laser beam addresses the $m_{J,e} = -1$ level. The resulting force is very similar to eq. (11), with an extra detuning term from the Zeeman splitting:

$$F_{\pm} = \pm\frac{\gamma}{2}\frac{\hbar k s_0}{1 + s_0 + \left(2\left(\delta \mp |\omega_D| \pm \mu'_B B/\hbar\right)/\gamma\right)^2}, \tag{15}$$

Note that this equation is a simplification for an atom with $g_J = 1$ and no splitting in the ground level. Such as the blue transition that we use in ^{88}Sr. Like with optical molasses, the laser is detuned below the transition. This means that atoms preferentially interact with the beam that oppose their direction of travel, due to the Doppler effect. Atoms at position $x' > 0$, as illustrated in fig. 5, are more likely to interact with the σ_- beam. This is because at that position, $\delta_- < \delta_+$. The opposite is true for $x' < 0$. The combined result is that atoms are slowed down, and pushed toward the center of the trap. With typical accelerations on the same scale as for cooling without Zeeman splitting. The maximum accelerations achievable here, using the blue transition, is 4 orders of magnitude larger than g, the acceleration due to gravity. Meaning spatial orientation of our setup does not need to take gravity into account.

2.3 Laser injection

The following is a brief explanation of injection locking, also known as optical seeding. It is a method used to make a diode laser copy the lasing characteristics of a reference laser. A laser diode is effectively a small cavity with a mirror on one side, a gain medium in the middle, and a partially transparent mirror on the emitting side. Diode lasers can achieve optical outputs of hundreds of mW. However, high power diode lasers usually do not have the required frequency stability for use in many experiments. Laser systems that fulfil the frequency stability requirements are typically expensive and more complex, and for our purpose they also have insufficient optical power. Injection locking works by coupling a small amount of light from a reference laser, called the parent or master laser, into a diode laser, called the child or slave laser. This injected light interacts with the gain medium of the child diode laser and induces stimulated emission. In effect, starting the lasing process at a specific frequency and competing with other possible modes inside the diode cavity. This results in the child laser copying the frequency and linewidth of the parent laser[12]. However, several factors influence this process. A diode laser has a broad gain spectrum and will naturally tend towards lasing at one or more frequency modes. Further, this gain spectrum is dependent on the temperature of the diode, as well as the current driving the diode. The temperature of the diode changes the length of this cavity and thus affects the resonant frequencies of the cavity [13]. This leads to temperature dependence of the gain spectrum. The driving current changes the carrier density in the gain medium. Resulting in a change in the refractive index of the gain medium, in turn resulting in a change in resonant frequencies and a shift in the gain profile[13]. The tuning of the diode close to resonance with the parent laser is often achieved by altering the diode current. The detuning range where injection is possible depends on the injection ratio, as well as the specific gain profile of the diode[14]. The injection ratio is the ratio between injected photons and photons from the diode. For the blue Nichia diode, used in our experiment, the injection ratio is typically on the order of $1-3\%$, with a typical output of $150mW$, a maximal achievable output of $500mW$ and typical injection power of $4-5mW$. The effective injection ratio also depends strongly on mode matching the injection beam to the child output beam, i.e. the injection beam has to be overlaid precisely with the diode beam, matching path and shape. Mode matching ensures optimized coupling of the injection laser into the diode cavity. For bad alignment, higher injection power is needed, or injection can be altogether impossible. In order for injection to work, the detuning between the child laser diode and the injection laser has to be on the order of a few GHz.

2.4 Squash locking: beam shape as a measure of injection quality

This section describes the theory of squash locking. A method used to enhance the stability of the injection locking method and potentially make a slave laser follow large frequency sweeps or steps. It is a cheap method of monitoring injection quality, and also easy to implement on existing laser systems with minimal impact. Squash locking was developed by F. Diorico et. al. at Institute of Science and Technology Austria[15]. As described in section 2.3, injection locking involves aligning a beam from a reference laser into a diode. Then, with the correct choice of diode driving current, the diode cavity will match the injected frequency and the reference laser will couple into the diode cavity. The beam from the reference laser also contains small components of higher order transverse electrical modes (TEM). For the purposes of squash locking, we are interested in the fundamental mode, TEM_{00}, and the small components of a second order mode, TEM_{02}, as illustrated in fig. 6.

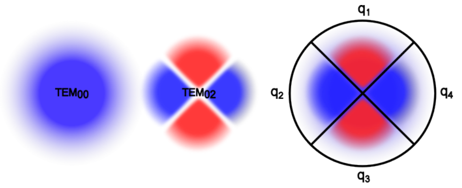

Figure 6: Fundemental Transverse Electric Mode (TEM_{00}) on the left. TEM_{02} in the center. On the right, modes overlaid, including quadrature sections. When both modes are present in a laser beam, shifts in relative phase between the two modes causes change in beam shape.

For a horizontally elongated beam, the TEM_{02} lobes marked in red will have opposite phase of the TEM_{00} mode, while the lobes marked in blue will have the same phase. This causes destructive interference between the red lobes and the fundamental mode, and constructive interference between the blue lobes and the fundamental mode. When the diode laser is injected, the TEM_{00} mode couples into the diode cavity. But the TEM_{02} mode is reflected off the face of the diode, as they do not match the diode cavity. The light from the diode will match the frequency of the injected light. But it will get a phase shift if it is slightly off resonance from the diode cavity. The result is that the interference between the reflected TEM$_{02}$ light and the emitted light from the diode will depend on the diode cavity detuning. Meaning a measurement of the beam ellipticity reveals information about how far the diode is detuned from the reference laser. I.e. how well the laser is injected. This measurement can be done simply by separating the beam in 4 quadrants, as illustrated on the right in fig. 6, and the calculating the ellipticity, β, using:

$$\beta = q_1 + q_3 - \epsilon \left(q_2 + q_4 \right), \tag{16}$$

where q_1, q_2, q_3, q_4 is the power in each quadrant and ϵ is a correction factor used to set the ellipticity to $\beta = 0$ at the injection point. This correction is needed since the beam is not necessarily perfectly circular when injected. As such, the method can be used to measure changes in injection quality, but it can not be used to locate the exact point where the diode is on resonance with the parent laser. But when that point has been located through other means, the β signal can be used to measure drifts in injection quality. It is also an asymmetrical function, so it can be used as an error signal. Since the diode resonance is changed by the diode current, the error signal β can be used as feedback to the current and used to correct for drifts.

2.5 NICE-OHMS

The following is a brief outline of the Noise Immune Cavity Enhanced Optical Heterodyne Molecular Spectroscopy (NICE-OHMS) method. It is included here as it is one of near future targets for the experimental setup. However, no work in this thesis involves this method. Instead, the work relates to preparing atomic beams for use in NICE-OHMS and perhaps, later on, other spectroscopic methods.

NICE-OHMS is a method developed to achieve high sensitivity measurements while suppressing noise. High sensitivity is critical for continuous atomic clocks, as the number of atoms in the cavity is expected to be much lower than in a discrete system, as atoms are not trapped inside the cavity.

NICE-OHMS utilizes an optical cavity to enhance the interaction between a spectroscopic sample and the laser used for probing. In our case, we are interested in interrogating the red $^1S_0 \leftrightarrow {}^3P_1$ transition in ^{88}Sr. The introduction of a cavity multiplies the interaction between the laser and the atoms with a factor proportional to the finesse of the cavity. This method alone is called Cavity Enhanced Absorption

Spectroscopy[16]. However, the introduction of a cavity also introduces additional noise. Any changes in cavity length, introduced by mechanical noise or thermal fluctuations, affects the absorption signal. To avoid this, a separate method is added to the experimental approach. Frequency Modulation (FM) works by adding additional frequency components, called sidebands, to the laser. The interference between the fundamental mode and the two sidebands results in a beat signal. The demodulated beat signal is zero, as the interference from either sideband cancel out. However, any interaction between atoms in the cavity and the central mode, called the carrier, results in a phase shift imposed on that mode. The resulting beat signal, when demodulated, now has a frequency proportional to the shift imposed by the interaction[17]. Any phase noise introduced by mechanical vibrations or thermal fluctuations have the same effect on the sidebands as on the fundamental mode, as they travel the same path and interact with the same optical elements. Meaning, the noise cancels out in the beat signal. Only the phase difference imposed by atomic interaction is left. For this to work, the sidebands have to be far enough in frequency from the atoms to not interact with them. But they also need to be able to couple into the cavity. The solution is to detune them by ± the FSR of the cavity. This means that they couple just as effectively into the cavity as the fundamental mode. And any drift in cavity length will affect coupling efficiencies equally. And any drift or noise in path length, in the cavity or otherwise, will impose the same phase shift on all frequency bands[17]. Resulting in no change to the signal.

3 Experimental setup and results

This chapter contains the experimental setup and results. The first sections give a brief overview of the larger experimental setup that this thesis was a part of. The subsequent sections are more comprehensive descriptions of the experimental work done by the author.

3.1 Experimental overview

The experiment is designed to do continuous spectroscopy of a cold strontium beam. The strontium beam originates in an oven, containing a metallic sample of ^{88}Sr, as illustrated in fig. 7. It is heated to about $500°C$, resulting in atoms evaporating and leaving the oven through a small nozzle. It then goes through a series of cooling stages. The atomic beam at the oven nozzle is divergent, resulting in a loss of atoms as they do not hit the port into the Zeeman slower, or they hit the inside of the Zeeman slower tube. A 2D optical molasses, placed at the oven nozzle, cools the atoms in the y and z-directions. In effect collimating the atomic beam partially, in order to increase the atomic flux through the Zeeman slower. The Zeeman slower works as described in section 2.2.3. The purpose here is to slow the atoms down in the x-direction. This results in longer interaction time for the atoms in the MOT region. The details of the atomic cooling and deflection in the MOT chamber is described in section 3.3, but in summary, the atoms are cooled and deflected into the cavity chamber, where an optical cavity is mounted. The spectroscopic interrogation takes place in the optical cavity, as outlined in section 2.5. The optical axis of the cavity is aligned along the z-axis. The purpose of all experimental components and techniques along the atomic beam path is to ensure that as many atoms as possible arrive in the cavity waist region. With μK temperature along the cavity axis.

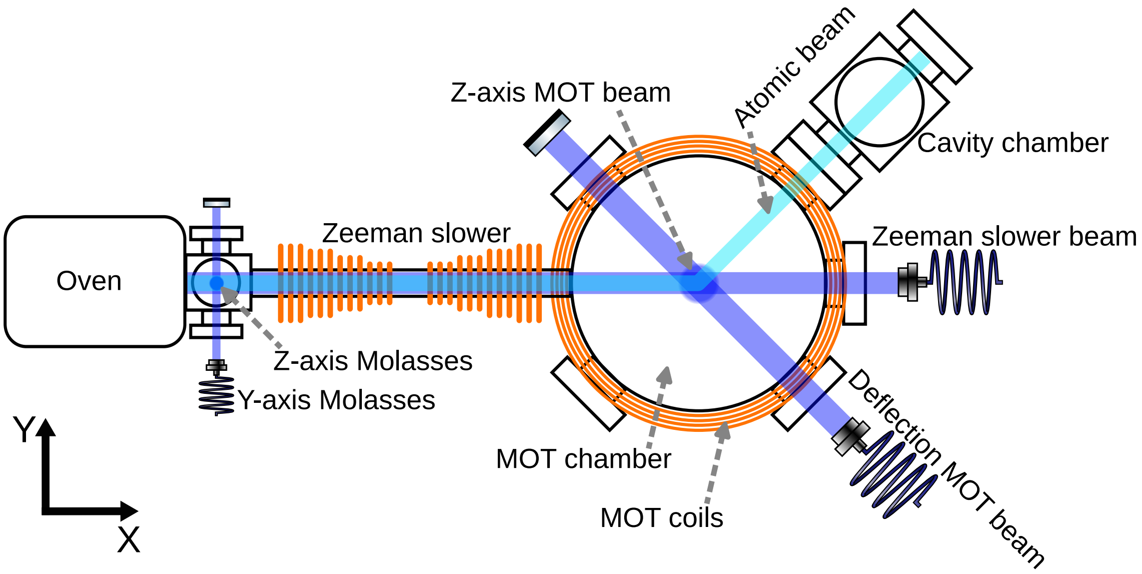

Figure 7: Top view of the experimental setup. A metallic sample of ^{88}Sr is evaporated in an oven and exits the oven through a small nozzle pointing towards the Zeeman slower tube. The atomic beam is partially collimated at the oven nozzle by use of optical molasses. Then, a Zeeman slower slows the atoms down before they enter the MOT chamber. In the MOT, the atoms are cooled and deflected into a separate chamber, containing an optical cavity. In the cavity, spectroscopic measurements are done.

The purpose of deflecting the atoms into a separate chamber is to isolate the spectroscopic measurements from optical disturbances. In a discrete atomic clock, the MOT and Zeeman slower beams has to be turned off when spectroscopic measurements are taken. Otherwise, those beams would disturb the measurements. In a continuous experiment, the cooling beams can not be turned off. So instead, the atoms are isolated spatially to avoid optical noise.

3.2 Injection sources and frequency chain

This section gives a brief overview of the different laser frequencies that are needed for the different atomic cooling stages. An overview of all the blue lasers used in the experimental setup can be seen in table 1. The reference laser is an ECDL laser from Toptica. This laser is locked to a vapor cell containing Strontium atoms. The locking scheme is Doppler Free Saturation Spectroscopy. A discussion of this method can be found in [11]. The laser is locked with a detuning of $-120MHz$ from the blue transition. This laser is called the Grandparent laser. The Parent laser is a diode laser, that is injected from the Grandparent. The output from the Parent laser is then split and frequency shifted several times, using acousto optical modulators. One laser beam is used to inject the MOT laser. Another laser beam injects the Zeeman laser. Their respective detunings are in table 1. Both of those lasers are also diode lasers. Finally, a beam from the parent board is shifted back to resonance and is used to probe the atoms for various measurements. For instance, the fluorescence imaging in section 3.3.4.

Laser	**Type**	**Relation**	**Stabilization scheme**	**detuning**
Toptica DL pro	ECDL	Grandparent	Doppler free saturation	-120MHz
Parent board	Diode	Parent	Injection from Grandparent	-120MHz
MOT board	Diode	Child	Injection from Parent	[-30,+15]MHz
Zeeman board	Diode	Child	Injection from Parent	[-500,-300]MHz

Table 1: An overview of the blue lasers used in the experiment and their respective frequency detunings.

3.3 Atomic deflection

This chapter describes the deflection of the strontium beam and the different elements involved in the deflection. After the Zeeman slower, the atoms arrive in a larger vacuum chamber with diameter $21cm$. This MOT chamber is illustrated in fig. 8. A set of large coils are set up around the chamber in an anti-Helmholtz configuration. This results in Zeeman-splitting of the $^1P_1$ state of the strontium beam and allows for cooling and compression of said beam, as described in section 2.2.4. The MOT has cooling lasers along 2 axes, that intersect at the center of the MOT chamber. Both retro-reflected and rotated in polarization at the reflection, using two passes through a quarter waveplate. One is perpendicular to the atomic beam. This laser beam cools and compresses the atomic beam, like described in section 2.2.4. It is oriented out of the paper plane in fig. 8, along the z-direction. The second axis of the MOT is drawn in blue as the deflection MOT laser beam in fig. 8. This laser beam is incident on the atomic beam at a 45° angle. This results in the atomic beam being deflected into the cavity chamber. This cavity chamber is mounted on the MOT chamber at a 45° angle relative to the x-axis of the overall setup. The deflection can be described in terms of vector decomposition. At the center of the MOT, we transform the atomic velocities from the xy system to a system that is rotated 45°. This system is denoted $x'y'$ in fig. 8. The velocity component parallel to y' is slowed in the MOT to $v_{y'} \approx 0$, and the atoms travel into the cavity chamber with velocity $v_{x'} = v_x/\sqrt{2}$. All this assumes that sufficient cooling is achieved in the time that the atoms interact with the MOT. Recent results by Julian Robinson-Tait, taken with this setup, suggest that atoms faster than $40 m/s$ are not deflected into the cavity chamber. Note that this model of deflection is simplified. It only holds for atoms traveling through the center of the MOT. A full model of the system can

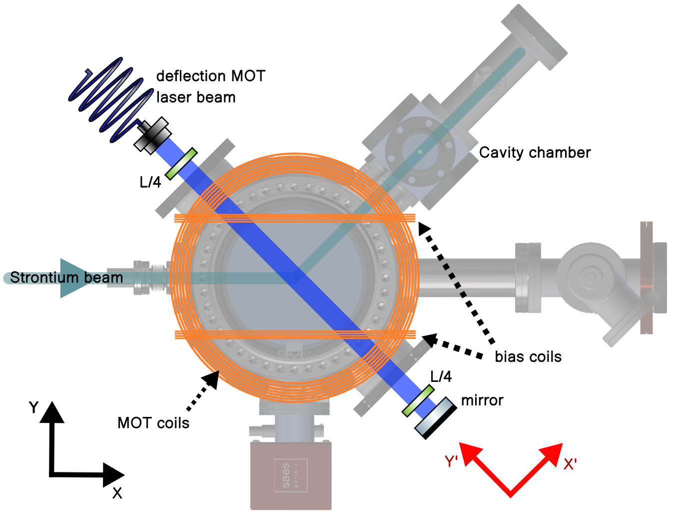

Figure 8: Top view of the MOT chamber, including the deflection scheme.

be treated as a form of lensing, resulting in focusing of the atomic beam. This model is not included here, but the need for such a model is apparent in section 3.3.6.

3.3.1 Building an injected diode laser for atomic deflection

Fig. 9 shows a schematic of the diode laser breadboard that was set up to provide optical power to the 2D MOT and the optical molasses at the oven nozzle. The laser is injected with 4mW of optical power, coming from the parent laser. With an optical output range of $[200, 300]mW$, this is an injection ratio on the order of 2%. The output of the diode is split several times. With the deflection MOT receiving 50% of the power. The other half is divided between the MOT in the z-direction, and the optical molasses. The characteristic lasing curve of the diode is included with the schematic in fig. 9. Coupling efficiencies for the fibers are all in the $40-50\%$ range, when aligned properly. The output from the laser diode is naturally elongated along one axis[13]. An example of the elongated beam profile can be seen in fig. 10. The first image is the laser beam, when the diode is not injected. In that case, the laser has multiple frequency components. The second image is the injected case. Here, a vertical pattern emerges. Likely the result of etaloning, when the laser becomes single frequency. The third image shows the intensity difference between the two. Horizontal bands of higher and lower intensity emerge. This is enough of a difference, that fiber coupling efficiencies can change by up to 8 percentage points between injected and uninjected. We are coupling the beam into several different optical fibers. A higher coupling efficiency is achievable with a circular beam shape. For this reason, the first components in the laser beam path is a cylindrical telescope with a 1 : 2.5 ratio. The optical fibers are single mode, polarization maintaining. The output of the fibers has a Gaussian beam profile. This output into the deflection

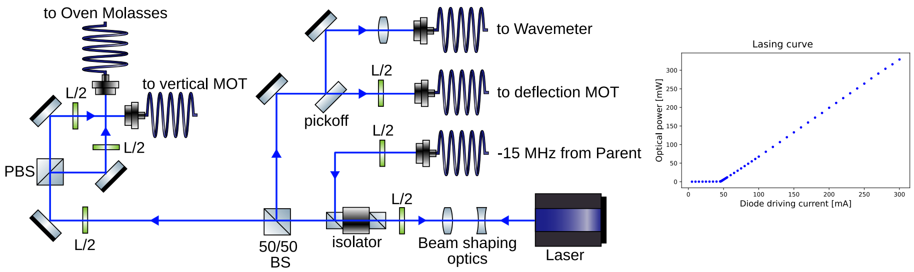

Figure 9: Schematic of the laser that provides power to the MOT and the oven molasses. The lasing curve for the diode is included on the right.

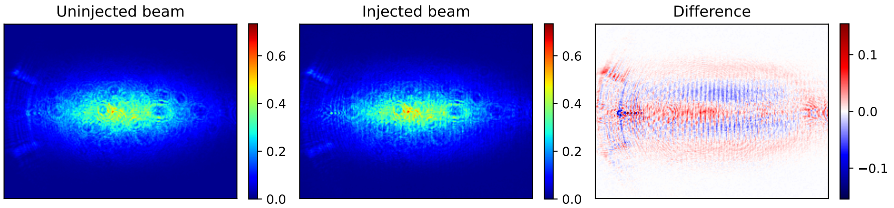

Figure 10: Laser beam profile as imaged by the camera in fig. 20. The first image is the beam when the optical seed is blocked. The second image is an example of the laser beam when injected. The third image is the difference between the two.

MOT is collimated using a combination of a $f = -100mm$ lens placed at a distance of $85mm$ from the fiber, followed by a $f = 100mm$ lens, $45mm$ after the first lens. This results in a beam with FWHM of $30 \pm 2mm$.

3.3.2 MOT main coils

This section describes the setup of the MOT coils, that provide the magnetic field responsible for Zeeman splitting in the MOT chamber. Two large circular electromagnetic coils, with diameter $d = 230mm$, are mounted outside the MOT chamber. Denoted as MOT coils in fig. 8. One below the chamber, and one above, with a distance of $d = 115mm$. They are connected in series, but with opposite current, such that they are in an anti-Helmholtz configuration. The resulting magnetic field is illustrated in section 2.2.4, fig. 4. With the available power supply, limited to $15V, 400A$ the maximum achievable magnetic field gradient along the z-axis is approximately $24.3G/cm$. Assuming the field gradient is linear from the center of a coil to the center of the MOT. The field gradients in the xy-axes are half the value of the field gradient along z, i.e. $12.1G/cm$. [11]

3.3.3 MOT bias coils

The following is a description of the secondary coils, that were set up to correct for possible misalignment in the MOT coils. Precisely aligning the MOT is important in order to cool down the atomic beam and redirect it into the cavity chamber at the correct 45° angle. The magnetic center of the anti-Helmholtz coils have to be aligned with the center of the atomic beam, as well as the laser beams used in the MOT. If these three elements do not align properly, the MOT will not cool as effectively as possible or the atoms will not travel into the center of the cavity chamber. The laser beam can be both translated and directed from outside the chamber. However, moving the anti-Helmholtz coils around is not practical, since they fit tightly around the MOT chamber. Instead, secondary coils are added to be able to offset the magnetic field. These are the bias coils, set up in pairs, to apply a uniform bias to the magnetic field. This allows us to move the center of the MOT field along the symmetry axis of the bias coil pair. To achieve a uniform field, these coils would ideally be in a Helmholtz configuration [18]. This ideal configuration can be seen in fig. 12. The bias coils for the z-axis were made with a radius of $R = 15cm$. They had to be mounted on top of the main coils, so the minimum distance they could be mounted was $d = 20cm$. A matching radius of $R = 20cm$ would be impractical, as it would impair placement of other experimental equipment. Meaning, they are not in an ideal Helmholtz configuration, resulting in a bias field that is not maximally uniform. Further, circular coils are not practical on all axes of the MOT chamber due to the shape of the Chamber. Instead, the bias coil pairs for the y-axis were found to be easier to place if wound in a rectangular shape, like the one seen in fig. 13. The choice of measurements of the rectangular coils were partially constrained by other equipment surrounding the MOT chamber. The possible measurements closest to the ideal configuration were coils with $[a = 28cm, b = 22cm, d = 15cm] \pm 0.5cm$. With a being aligned along the x-axis and b along the z-axis. The measurements were mostly constrained by considerations of placing optical elements around the MOT chamber. This rectangular set of bias coils are shown in fig. 8, denoted "bias coils". It was determined that no bias field was necessary along the x-axis, since atomic beam alignment into the cavity chamber only required 2 degrees of freedom. Since neither of the bias coil pairs had ideal geometry, measurements were taken to determine whether the resulting field was approximately uniform. Using the Biot-Savart law, the magnetic field strength was calculated along the center line of both coils. These calculations showed that the circular coils were the furthest from constant along the center line. For this reason, the circular coil pair were measured physically. The logic being that if they were sufficiently uniform, the same would be the case for the rectangular coil pair. Measurements of the magnetic field strength were taken in a $5 \times 5 \times 5cm$ cube in steps of $1cm$. The measurements were taken before the coils were mounted to the MOT chamber, with the coils held at the same distance as on the MOT chamber. Measurements are only in the direction along d as in fig. 12. The field strength varies within a range of $[10.059, 10.416] \pm 0.05Gs$.

This is a 3.55% difference from minimum to maximum. The magnetic field gradient varies between $[-0.141, 0.148]Gs/cm$. Plots of the magnetic field in the center plane along all 3 axes can be seen in fig. 11, with the gradient overlaid as arrows. Note that this is the field strength along d, according to fig. 12. The small fluctuations were deemed acceptable, since the blue transition is relatively broad. So a few percent of variation in magnetic field should be negligible. Considerations for the strength required in the bias field were as follows: Worst case, the MOT chamber may be rotated off the Zeeman cooler axis by up to 1°, resulting in a distance between the center of the atomic beam and the geometric center of the MOT chamber of up to $2mm$. The MOT coils may also be misaligned by up to $5mm$, with regard to the geometric center of the MOT chamber. Assuming any and all misalignments are added, the magnetic field would need to be shifted by $7mm$ along the y-axis to ensure that the center of the magnetic field intersects with the center of the atomic beam. In our setup, the magnetic field has a maximum gradient of $12.1G/cm$. Meaning a field of $12.1G$ can offset the field center by $1cm$. The available power supply for the bias coils was limited to $32V, 3.2A$. This can provide sufficient power as long as the coil design take these limits into account. At maximum current, 70 windings should result in a field of approximately $14G$. Providing sufficient strength to offset the magnetic field, if all misalignments add up. In practice, the MOT coils are typically run at $10A$, giving $8.9G/cm$. So the bias coils should be able to provide sufficient field offset. With a max current of $3.2A$, using enameled copper wire with a cross-section of $1.18mm^2$, this would result in a total power consumption of $16W$ for the coil pair. Meaning the coils could be passively air-cooled even at maximum current.

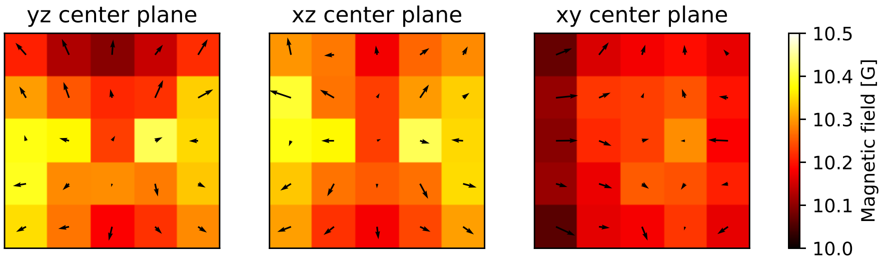

Figure 11: Heatmap of the magnetic field along z in the center planes of the $5 \times 5 \times 5$ grid, where the field was measured at the center of the rectangular offset coil pair. Grid spacing is $1cm$. The z-axis is aligned with d from fig. 12

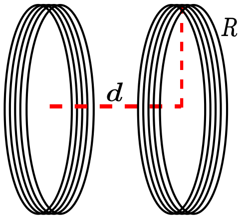

Figure 12: Circular electromagnetic coils arranged in a Helmholtz configuration. Both coils have radius R and are placed at distance d. For $d = R$ the magnetic field is as uniform as possible, for this configuration, along the center axis[18].

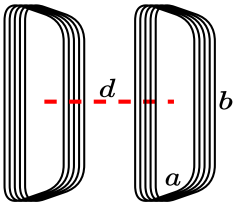

Figure 13: Rectangular electromagnetic coils with side lengths a and b, set up in series. For $a = b \approx 1.8365d$ the magnetic field is as uniform as possible, for this configuration, along the center axis[19]

3.3.4 Tuning atomic deflection

The following section describes how the atomic beam was deflected into the cavity chamber. And how the bias coils along the y-axis were used to tune the deflection. For these experiments, the MOT coils were run at $10A$, resulting in an approximate field strength gradient of $8.9G/cm$. Two probe beams, on resonance with the blue Sr transition, were sent into the smaller vacuum chamber, denoted cavity chamber in fig. 8. Fig. 14 shows the two probe beams, travelling right to left, inside the dashed green boxes. The camera was placed such that the view is into the chamber from above. I.e. negative z-direction. Each beam has $0.1mW$ optical power. The fluorescence shows the presence of Sr atoms. When this data was taken, the cavity had not yet been placed in the chamber, allowing for imaging from both axis perpendicular to the atomic beam. The vacuum chamber has windowed ports with an inner diameter of $50mm$. The inner edge of the window closest to the camera has been marked with a dashed yellow line. The edge of the window behind the atoms have been marked with a dashed red line. The probe beams were equidistant from these windows. So the average diameter of the two dashed circles have been used to translate from pixels to mm. The example image in fig. 14 has been taken with no bias field applied. The fluorescence inside each green box was summed along the vertical axis of the image. The resulting distributions have been plotted on the right. A background image with no atoms present was taken and subtracted. Each distribution has been rescaled to a maximum of 1.

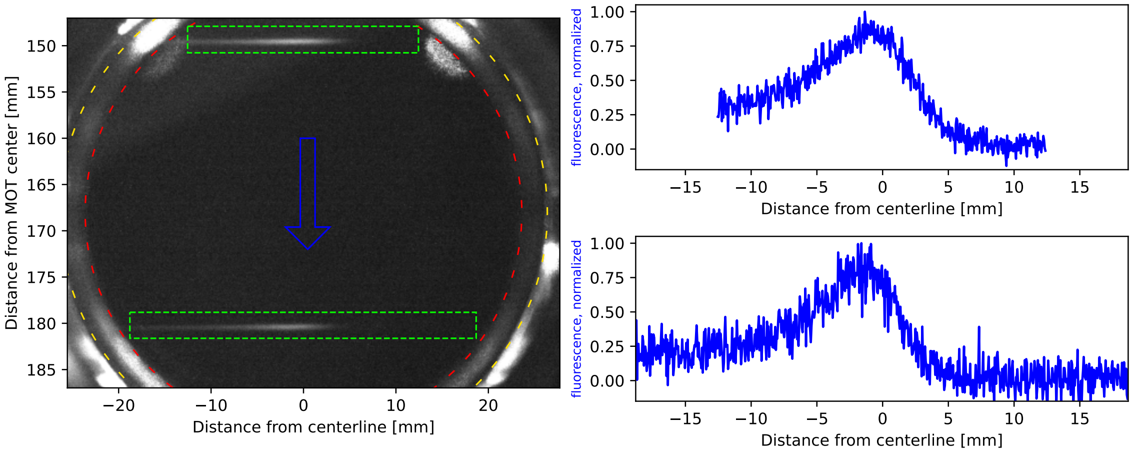

Figure 14: Atomic fluorescence, marked in green boxes, in the cavity chamber, before cavity was installed. Fluorescence summed vertically, rescaled to a maximum of 1 and plotted on the right. Data captured by Julian Robinson-Tait.

Next, the current to the bias coils in the y-direction was manually stepped in steps of $0.5A$, in the range $[-3, 3]A$. Fig. 15 show the resulting distributions inside the upper box in fig. 14. Averaging has been applied with a width of 21. For the figure, each distribution has been offset with the current to the bias coils. In the first and the last images in the series, the atomic beam was clipped by the viewport, so the maximum is not visible. Notice how the distribution of fluorescence seems similar for the different currents, just offset sideways.

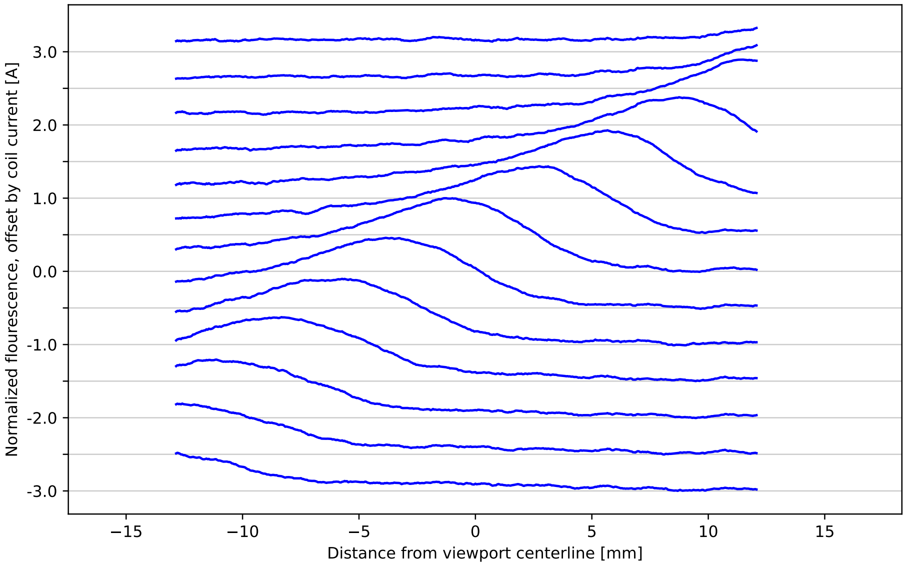

Figure 15: Smoothed distributions of atomic fluorescence in the top box in fig. 14. Rescaled to maximum of 1. Offset vertically by the current in the bias coils. Notice that the distributions are shifted sideways proportionally to coil current.

Fig. 16 show the same fluorescence distributions, only from the lower box in fig. 14. The box is slightly wider in this case. Resulting in more distributions having a visible maximum.

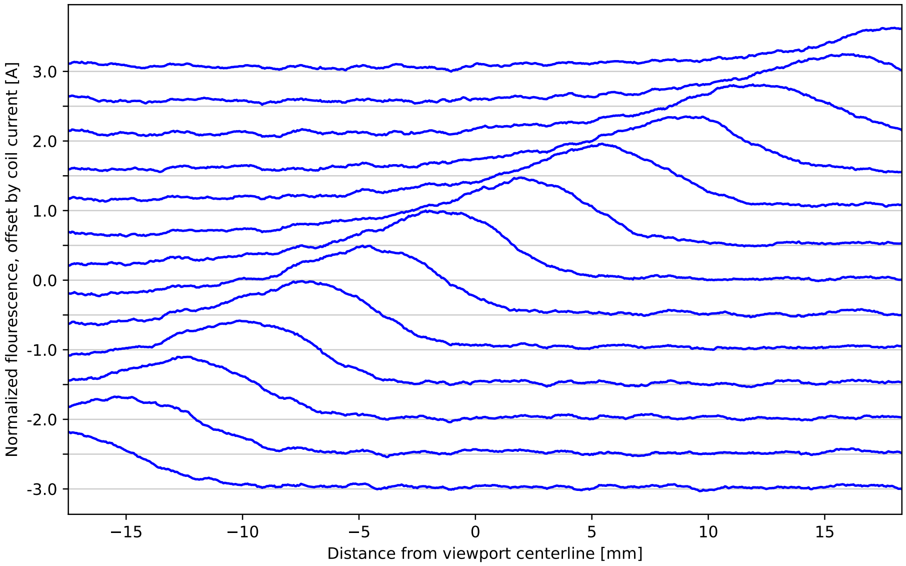

Figure 16: Smoothed distributions of atomic fluorescence in the bottom box in fig. 14. Rescaled to maximum of 1. Offset vertically by the current in the bias coils. Notice that the distributions are shifted sideways proportionally to coil current.

The position of the maximum of each distribution, relative to the centerline of the viewport, has been plotted in fig. 17. The uncertainty of each position is given as the width of the smoothing window, translated from pixels to mm. Trend lines for the two beams intersect around $-2.5mm$, meaning left of the center of the chamber. This could be because the atomic beam does not originate at the geometric center of the MOT chamber, rather a little further from the Zeeman slower opening. However, with the uncertainties of the position of the fluorescence maxima, it can not be confidently concluded. As discussed in section 2.2.4, it is also likely that atomic deflection angle is dependent on the atomic velocity in the x-direction. This could result in the apparent point of origin of the atomic beam being different for different velocity groups. Looking at any one of the distributions in fig. 16, the fluorescence is practically zero in the tail on the right side of the maximum. The fluorescence in the tail on the left, remains non-zero almost across the entire viewport. This behavior is consistent with deflection angle being at least partially inversely proportional to longitudinal atomic velocity.

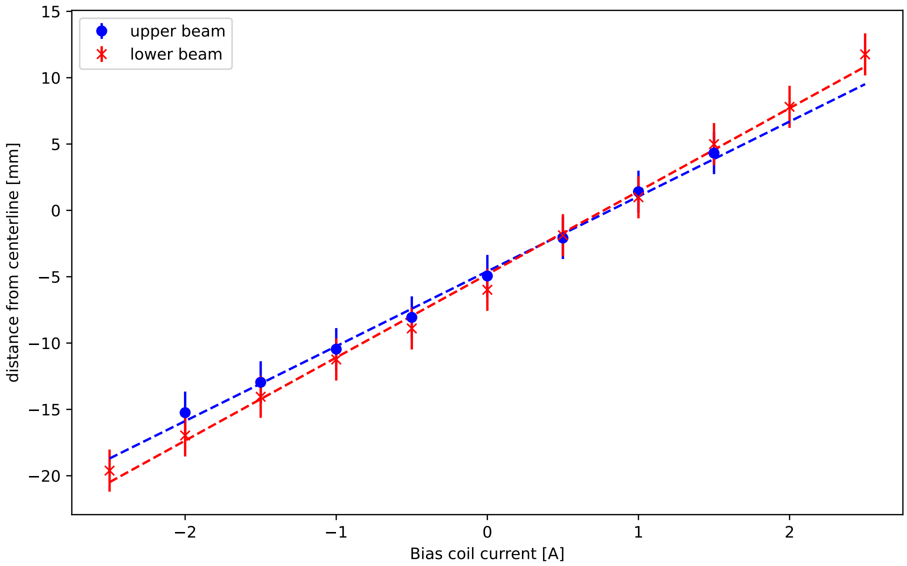

Figure 17: Location of maximum value for each distribution in fig. 15 and fig. 16. Uncertainty is half the width of the smoothing window. Trend lines are plotted in dashed lines.

In fig. 18, only the data points with defined maxima in both beams have been included. The uncertainties are the same, but have been excluded since they overlapped between neighboring points. The figure show dashed lines between the maxima from a given image. This line extends towards the center of the MOT chamber.

In a simplified picture where the MOT chamber was perfectly positioned relative to the Zeeman slower tube, and the bias field only resulted in a different deflection angle, all lines would converge to a point at $(0, 0)mm$. Assuming imperfect alignment between MOT chamber and Zeeman slower tube, the lines would converge at $(y, 0)mm$. With the hypothesis of the magnetic bias field resulting in translation, the lines should all be parallel. Taking uncertainties into account, the lines are more consistent with deflection than translation. However, a combination of both phenomenon could also be possible.

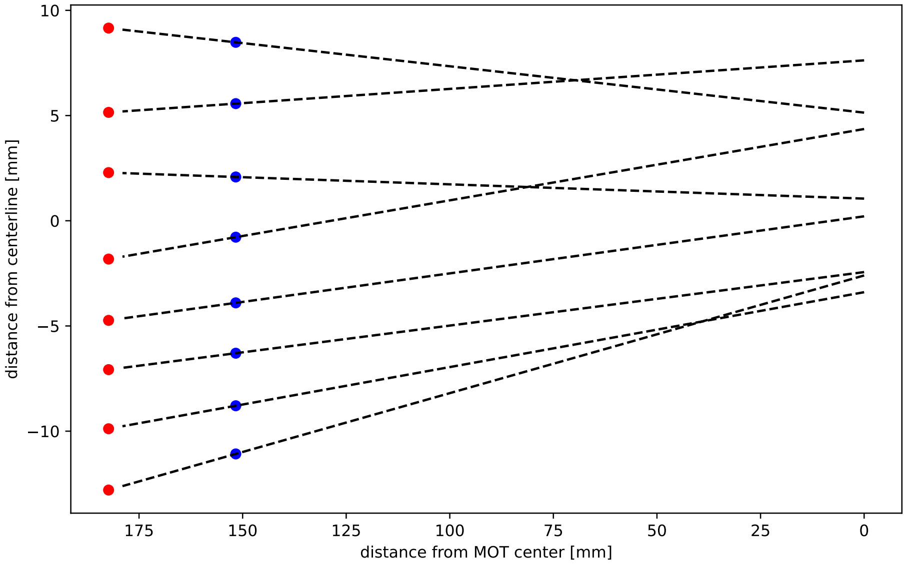

Figure 18: Maxima from fig. 17 plotted in x'y'-plane. Dashed lines point toward the apparent origin of the atomic beam.

3.3.5 Atomic flux estimation

The following is an estimation of the atomic flux in one of the probe beams described in section 3.3.4. The first step is calibrating the camera to obtain a scaling factor α, between camera bits and optical power. A beam of known power was directed into the camera, making sure that no pixels saturated. The optical power was divided with the sum of all pixel values in the image. Normalizing by exposure time and camera gain:

$$\alpha = \frac{P_{\text{calibration}} \cdot T \cdot 10^{G/20}}{\Sigma_{\text{bit}}}, \tag{17}$$

where $P_{\text{calibration}}$ is the known optical power into the camera, T is the camera exposure time, G is the camera gain in dB, and Σ_{bit} is the sum over all 8bit pixels. Next, the same relation is used to calculate how much optical power is captured in the actual fluorescence image:

$$P_{\text{image}} = \frac{\Sigma_{\text{bit}} \cdot \alpha}{T \cdot 10^{G/20}}, \tag{18}$$

making sure that values for T and G are from the relevant image. Next, we find the total optical output of the beam. The camera only captures a small solid angle of the emitted light from the atoms. So the total light scattered from the atoms is calculated as:

$$P_{\text{scattered}} = P_{\text{image}} \cdot 2\pi d^2/A, \tag{19}$$

where d is the distance from the camera to the probe beam, and A is the area of the lens aperture. We then calculate the average probe beam intensity as:

$$I = \frac{P_{scattered}}{w^2\pi}, \tag{20}$$

where w is the waist of the probe beam. Using eq. (2) and eq. (1), we calculate the scattering rate. Finally, we can calculate the atom flux as:

$$Q = \frac{P_{scattered}}{T\gamma_p E_{\text{photon}}}, \tag{21}$$

where E_{photon} is the energy of a single photon scattered from the blue transition. The most important numbers used in these calculations can be found in table 2. The atomic flux in the bottom of the two beams in fig. 14 was calculated to be $Q = (2.2 \pm 0.7) \cdot 10^4 s^{-1}$.

α	$\Sigma_{textbit}$	P_{image}	$P_{\text{scattered}}$	s_0
$1.2 \cdot 10^{-14} J/\text{bit}$	368829	$4.0 \cdot 10^{-13} J$	$1.6 \cdot 10^{-8} J$	1.25

γ_p	$E_{\text{photon}}(\lambda = 461nm)$	T	Q
$8.5 \cdot 10^6 s^{-1}$	$4.3 \cdot 10^{-19} J$	$200ms$	$(2.2 \pm 0.7) \cdot 10^4 s^{-1}$

Table 2: Atomic flux, Q, in the bottom of the two beams shown in fig. 14. Along with the most important parameters used in calculating atomic flux. Note that the bit sum is multiplied by 4 since the image was taken 2×2 binning with averaging, while the calibration image was taken without binning.

3.3.6 Atomic temperature in the cavity region

This subsection is an exploration of the transverse temperature in the atomic beam in the cavity chamber. The analysis uses the data presented in section 3.3.4. Since no model for the transverse atomic distribution has been developed, it was assumed that the central peak feature was approximately Gaussian, with some additional features. So the data was truncated around the peak and a Gaussian function was fitted. Five data sets had enough data on both sides of the maximum to reasonably fit a Gaussian. The truncated data sets and the Gaussian fits can be seen in fig. 19.

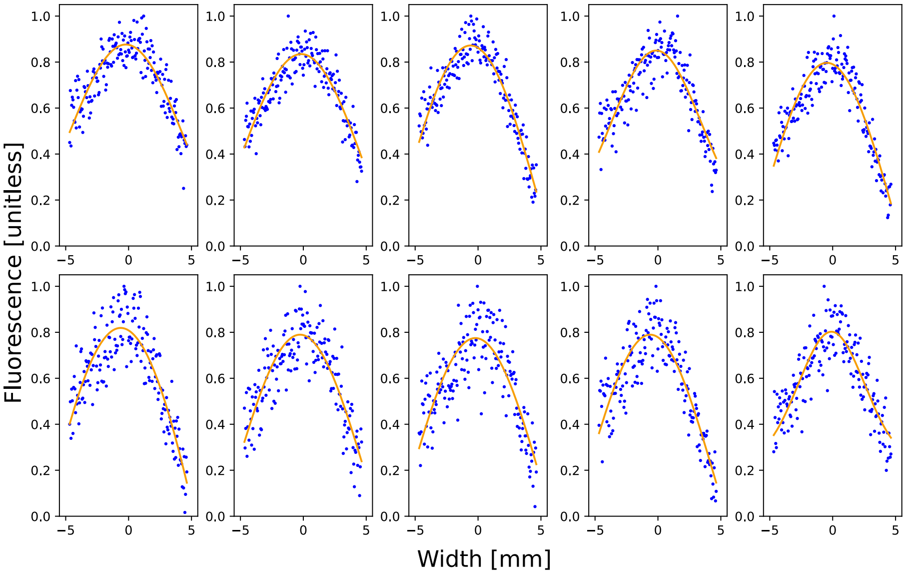

Figure 19: Fluorescence data in blue. Gaussian fit in orange. Data is truncated to only include area around maximum. Top row of plots are from the upper box in fig. 14. Bottom row of plots is from the lower box.

The FWHM of each fit is calculated and averaged for upper and lower box. Resulting in $\text{FWHM}_{\text{upper}} = 8.8 \pm 0.7mm$ and $\text{FWHM}_{\text{lower}} = 7.98 \pm 0.13mm$. Note that the distribution actually becomes narrower. The average change in position relative to the centerline of the cavity chamber is then:

$$\Delta y' = \frac{\mathrm{FWHM}_{\mathrm{lower}} - \mathrm{FWHM}_{\mathrm{upper}}}{2}, \tag{22}$$

and the transverse velocity is given as:

$$v_{y'} = \frac{\Delta y' \cdot v_{x'}}{2d}, \tag{23}$$

where $v_{x'}$ is the longitudinal atomic velocity, and d is the distance between the two laser probe beams, along x'. From there, the temperature is calculated as:

$$T = \frac{v_{y'}^2 \cdot M}{k_B}, \tag{24}$$

with M being the atomic mass and k_B being the Boltzmann constant. When doing error propagation for the temperature, the error from the FWHM measurements is the largest contributor by 7 orders of magnitude. In fact, the result, $2 \pm 3mK$ is unphysical, since we can not have negative temperatures. So instead of using conventional error propagation, assuming non-correlated parameters, the error is instead obtained by calculating T, using $\Delta y' \pm \sigma_{\Delta y'}$, resulting in asymmetrical errors. The resulting temperature is then $T = 2^{+4}_{-1.6}mK$.

3.3.7 Discussion of deflection results.

The central peak of the distribution is approximately $10 - 15mm$ wide, which matches reasonably well with the $16mm$ aperture of the Zeeman slower. But the left side of the distributions, corresponding to $< 45°$ deflection, extends to the edge of the detection window. Illustrating that not all atoms experience $45°$ deflection. This is likely atoms that are too fast to reach optimal cooling and deflection in the MOT. As such, their velocity along $y' \neq 0$.

When no bias field is applied, the center of the atomic beam is not deflected into the center of the cavity chamber. This suggests either incomplete cooling, or more likely imperfect geometric alignment between the Zeeman slower, MOT chamber and MOT beams. No framework has been presented to establish the theoretical relation between deflection angle and magnetic field bias. As such, the deflection results can not be directly tested against a numerical hypothesis. But for the small adjustments tested here, the change in deflection can reasonably be described as proportional to the bias field, as illustrated by fig. 17. In order to center the maximum of the atomic distribution in the cavity chamber, a current to the bias coils of approximately $0.9A$ was needed. Meaning that the bias coils should be sufficient for a magnetic field gradient with 3 times the slope. The measured atomic flux seems low. This could be due to poor optimization of the atomic beam, as this data was taken before some optimization steps. Or just as likely, it could be due to errors in the calculations. But at the time of writing, such errors remain elusive. The transverse temperature measured has large errors, but is compatible with temperatures expected from a blue MOT. The fact that the atomic distribution becomes narrower as the atomic beam travels away from the MOT suggests, that atomic lensing is happening. This phenomenon has not been modeled in this thesis, but can very briefly be explained by the fact that atoms away from the MOT center are cooled on a much faster timescale than the timescale to push the atoms to the center of the MOT[9]. So when the atoms move through the MOT on a timescale large enough for cooling, but too short for full compression, they will essentially have a small transverse velocity component towards the center of the atomic beam.

3.4 Squash locking

This chapter describes the implementation of the squash locking method outlined in chapter 2.4. The results of an initial test of the implementation is also presented.

3.4.1 Setup

A laser diode is set up in a diode housing. Diode current is controlled by a diode current controller, with a maximum current of $200mA$. A temperature controller maintains the diode temperature. A schematic of the optical setup can be seen in fig. 20. The first component along the laser beam is a beam sampler, which takes approximately 1% of the light from the laser and redirects it onto a camera sensor. The camera has no lens, only a 30dB neutral density filter to avoid saturating the sensor or causing damage. Following the beam sampler is a cylindrical telescope with a 1:2.5 ratio. This laser uses the same diode as the one described in section 3.3.1, so the same type of beam shaping optics are necessary to make the beam roughly circular. An example of the beam profile, before the beam shaping telescope, can be seen in fig. 10. An optical isolator is positioned after the telescope to ensure that reflections further upstream do not return to the diode, as such reflections can interfere with the diode's stability[20]. The isolator also has a side port that allows for a separate beam to be injected and enter the laser diode. An optical seed originating at the grandparent ECDL laser is input to this port and mode-matched with the diode to optimize frequency injection. Lastly, two more beam samplers are placed after the optical isolators: one for a fiber that leads to a high-finesse wavemeter, and another that couples into a scanning Fabry-Perot interferometer. The Fabry-Perot is described in more detail in section 3.4.2. The wavemeter is a HighFinesse wavelength meter WS-7. The camera image is captured using a Python script[1].

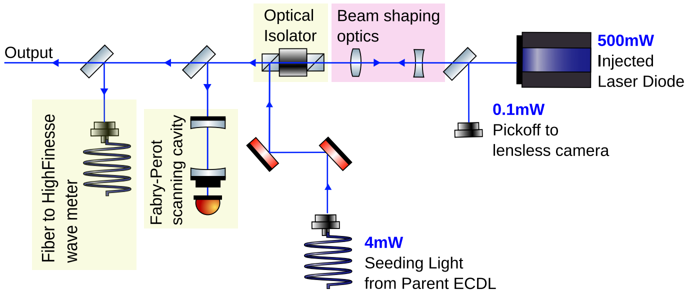

Figure 20: Schematic of the setup used for the squash locking experiment. The laser is frequency injected by light from the grandparent ECDL laser. A beam sampler redirects 1% of the diode light onto the camera sensor. In front of the camera is also mounted 30dB of neutral density filters to avoid saturating the camera sensor. The signal from the camera is analyzed in a Python script and feeds back to the laser diode current. The same script also saves traces from a scanning Fabry-Perot interferometer at regular intervals. A sample of the light also goes to a HighFinesse wavelength meter.

Component	*Model*
Diode housing	Thorlabs TCLDM9
Laser diode	Nichia NDB4916
Diode current controller	Thorlabs LDC202C
Diode temperature controller	Thorlabs TED200C
Camera	FLIR Blackfly S BFS-U3-31S4M
Wavelength meter	HighFinesse WS-7
Scanning Fabry-Perot interferometer	Thorlabs SA210-3B

Table 3: Major components used for the squash locking experiments.

---

[1] The script can be found at `https://github.com/Hooverboy/DigitalSquashLocking`.

3.4.2 Measuring frequency components of the laser

The following is a description of the scanning Fabry-Perot interferometer used to measure the frequency components of the laser. A schematic view of the Fabry-Perot is included in fig. 20. It is a confocal cavity with a Free Spectral Range (FSR) of $10GHz$ and a resolution of $67MHz$. The second mirror is mounted on a piezo element that allows us to modulate the length of the cavity with a sawtooth voltage signal from a signal generator. This changes the length of the cavity and changes the resonant frequencies that can exist inside. As the voltage modulation changes the length of the cavity, the different frequency components of the laser are resolved. The Fabry-Perot also has a photodetector behind the cavity. The photodetector is connected to an oscilloscope, providing the readable signal. An example of the oscilloscope signal can be seen in fig. 21. In blue is the modulating voltage to the piezo. In red is the signal from the photo diode. The trace was taken when the laser was injected. Note the vertical dashed lines and the two identical peaks between those dashed lines. The distance between these peaks is equal to the FSR of the cavity. But from the cavity signal alone, there is no way to know the their absolute frequence. The HighFinesse wavemeter can measure the frequency of the most intense component. Allowing us to determine the frequency of the highest peaks. Smaller peaks can then be mapped by the distance from the large peaks. But only up to a factor of $n \cdot \mathrm{FSR}, n \in \mathbb{Z}$. So any frequencies that are separated by an integer number of $10GHz$ are indistinguishable. The expected linewidth of the blue laser, when injected, is on the order of Hz and the linewidth of the Fabry-Perot cavity is given as $67MHz$ by the manufacturer. The peaks seen in this figure have linewidths on the order of $1GHz$. This is most likely the results of poor optical alignment into the Fabry-Perot cavity. The peaks also taper off slowly on the side facing higher voltage. This is not consistent with the expected spectral shape of the diode laser. The injection process should effectively transfer the spectral properties of the parent laser to the injected child laser, resulting in a narrow linewidth output[21]. The cause of this tail and the wider than expected linewidth, is likely bad optical alignment. No effort was made to mode-match the laser into the cavity. The cavity may also not be truly confocal, as a confocal cavity should be mode degenerate. But during alignment separate modes were apparent. However, given these imperfections, it is still a useful tool to qualify the power in the injection mode of the cavity, better than the wavemeter alone. Note also the presence of smaller peaks, indicating that while the diode was injected, a small part of the optical power was located in a different frequency than the injected reference.

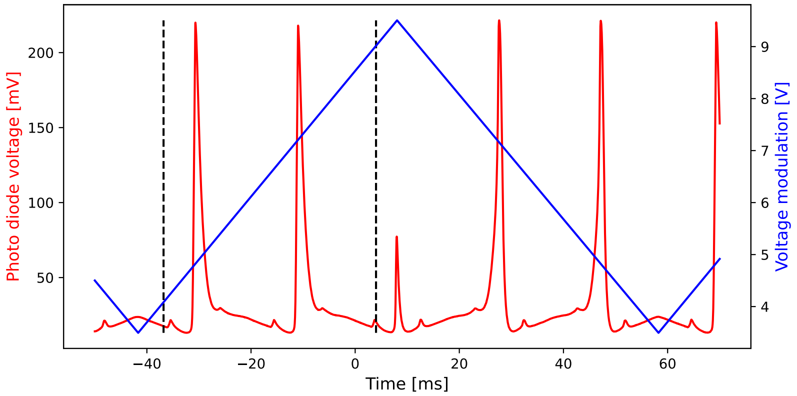

Figure 21: Example of oscilloscope trace from the photo diode of the Fabry-Perot (red), along with the voltage modulation to the piezo(blue). The cavity has an FSR of 10GHz and a resolution of 67MHz. The highest peaks represent the injected frequency the laser is lasing at. Note that there is also a small peak, representing a different frequency component.

3.4.3 Implementing squash locking

This section provides an overview of how an error signal for squash locking was obtained and how the locking was implemented. Instead of using a quadrature photodetector as in [15], the camera image is analyzed and used to calculate ellipticity. This analysis is done in a Python script that captures images at approximately 25 Hz. This Python script implements several features:

- A graphical User Interface (GUI)
- Measuring ellipticity
- Locking to ellipticity signal with Proportional-Integral (PI) control.
- Voltage output for current modulation
- Measuring optical power
- Logging and saving data, including oscilloscope traces

- Current scan for injection point search
- Removing image background
- Real time monitoring of lock

A screenshot of the GUI in use can be found in appendix A. To calculate ellipticity from the camera image, a square area of interest is placed in the image live view, such that is centered on the beam profile. The script divides the square area into 4 quadrants, like illustrated in fig 24 and sums each of those quadrants to obtain q_1, q_2, q_3, q_4 as in eq. 16. The user then finds an injection point and normalizes the ellipticity. This simply sets ϵ to the value that satisfies $\beta = 0$. This is done to correct for any initial power imbalance between the quadrants. Squash locking is implemented as a Proportional-Integral (PI) scheme to maintain $\beta = 0$. It does so by current modulation. Specifically, it communicates with a Red Pitaya microcontroller board to output a modulating voltage in the range $[0, 1.8]V$. This voltage is then input to the Modulation Input on the Thorlabs diode controller. This change in current offsets the gain profile of the diode and thus is able to affect the ellipticity. As explained in more detail in chapter 2.4. In addition to monitoring and maintaining injection, the script also logs data at set intervals. The most important features that are saved are:

- Ellipticity
- The separate quadrants
- Optical power
- Control voltage
- Time
- Oscilloscope trace from scanning Fabry-Perot cavity

With the use of this script, initial explorations of the squash locking scheme were done in the form of current scans over an injection point. Measurement of ellipticity and optical power was taken over a current descent as seen in fig. 22. The positive slope part of the zoomed in region in the inset plot corresponds to an injection point. This was determined by use of the wavemeter. In the injection region, the ellipticity is strictly increasing, apart from some noise. This slope is used as an error signal for squash locking. The 4 quadrants used to calculate ellipticity from the camera image can be seen in fig 24. Note that in this data set $\beta \neq 0$ at the injection point. This is because prior to obtaining the data, ellipticity was not normalized correctly at an injection point. This has been corrected later for the active locking experiments. The values of the 4 quadrants are plotted in fig 23.

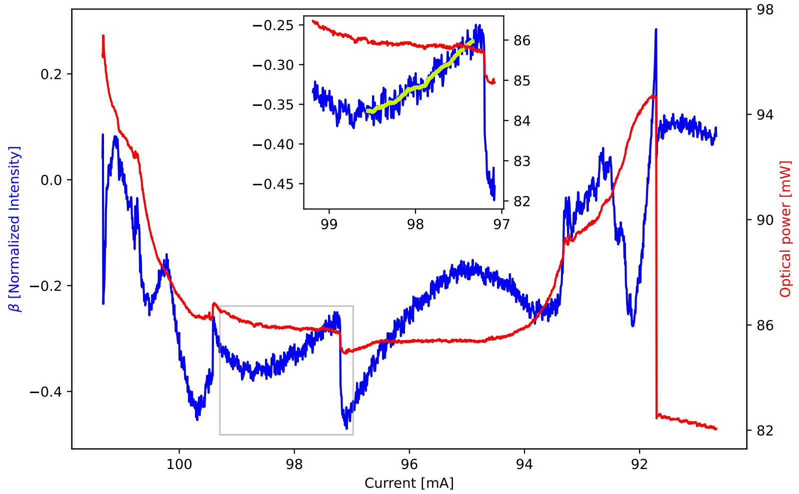

Figure 22: Current to the laser diode is scanned and ellipticity and optical power is monitored during the scan. The zoomed in region represents an area where the laser is injected. Specifically, the slope marked in light green. This slope is used as the error signal for squash locking.

This is in the injected region as zoomed in on in fig 22. Note that quadrant values q_1, q_3 are both increasing with decreasing current in the injected region. Since these contribute with positive sign to the increasing ellipticity, this is expected. However, q_2, q_4 contribute with negative sign. And according to the theory, they would both decrease when the ellipticity value increases. But q_4 is instead slightly increasing. This could be because the square used to calculate ellipticity has not been placed at the right position. Determining the position of the center of the laser beam was difficult.

Fig. 24 illustrates how the ellipticity evolves around an injection point. A background image has been taken at $\beta = 0$. Then images of the beam were taken at $\beta = 0.057, -0.107$, with the background subtracted. For the positive ellipticity as seen in a), the pixel values in quadrants q_1, q_3 are almost all higher than in the background. For q_2, q_4 it is a little more mixed. For negative ellipticity, shown in b),

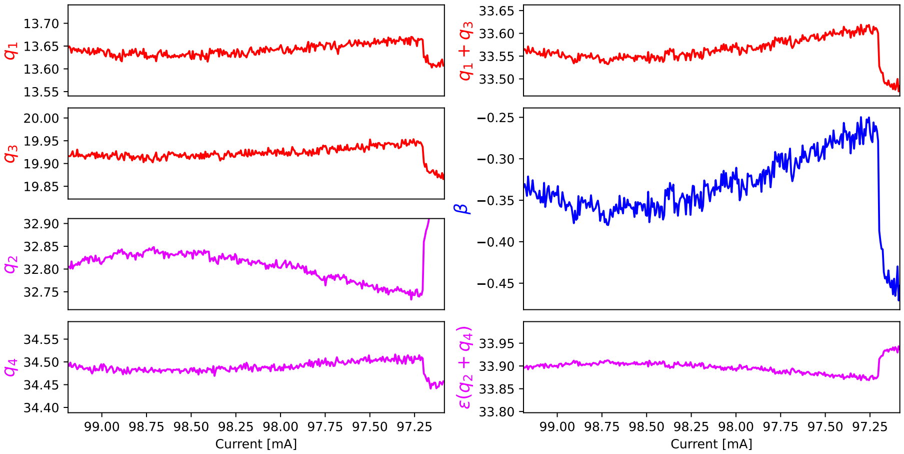

Figure 23: Plots off constituent parts of β from the zoomed in region in fig. 22. On the left are separated values for q_1, q_2, q_3, q_4. In the top right is $q_1 + q_3$. Bottom right is $\epsilon(q_2 + q_4)$. Middle right is β.

q_1, q_3 have decreased in value on average, but there are areas that have increased in intensity.q_2, q_4 also has a mix of values, with larger areas having increased in value.

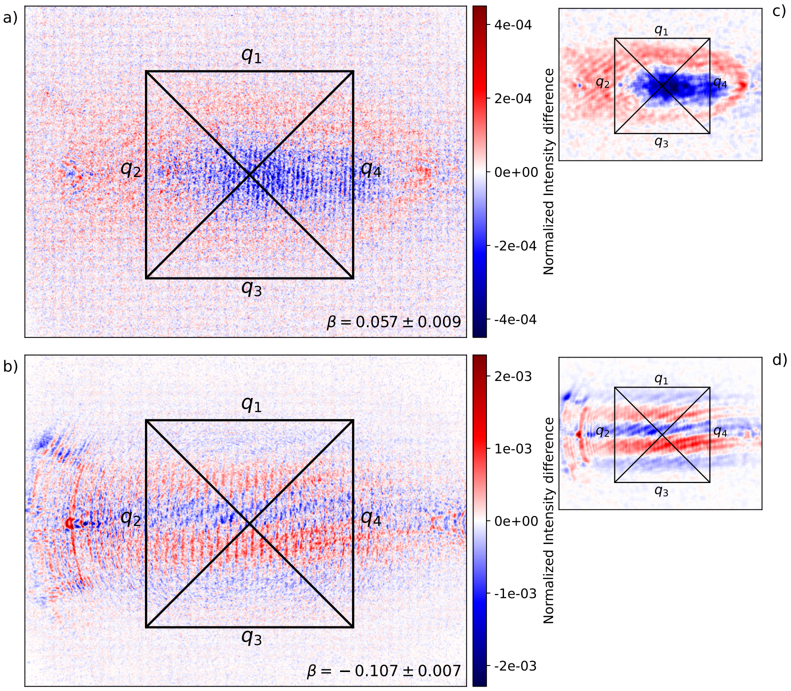

Figure 24: Images of the beam at both positive and negative ellipticity. A background image was taken at $\beta = 0$. This background has been subtracted from the images shown here. a) shows positive ellipticity, with c) being the same image with some smoothing applied for easier comprehension of which areas have increases and which have decreased. b) and d) show the same thing for negative ellipticity. Note the different color scale between the two images.

3.4.4 Squash locking measurements

Two primary data series were obtained to evaluate the feasibility of the squash locking scheme. For each series, the oscilloscope trace from the Fabry-Perot was recorded, along with the ellipticity and other parameters from the locking script, described in section 3.4.3, at 1-second intervals. In the first series, the laser is injected and monitored, but active maintenance of the injection is not performed. The experiment ran for two hours and the data is shown in fig. 25. Fig. 25d shows the spectrum over time, in logarithmic scale, to enhance visibility for any smaller frequency components. One vertical slice of this spectrum corresponds to the area between the two dashed lines in fig. 21. Fig. 25a shows the amplitude of the main frequency component. It remains almost constant, with only a small decrease over time. And a momentary drop after 115 minutes. Fig. 25b displays the ellipticity within the same time frame. The ellipticity graph indicates potential issues with the squash locking method. According to the spectrum, the laser stays injected and single frequency, while the ellipticity drifts. This could potentially mean that ellipticity in this case is not solely affected by how close the laser is to perfect injection. It could also be the case that temperature drifts slowly makes the gain curve shift. Which according to the squash locking theory would result in a change in ellipticity. The laser can still remain injected and single frequency despite this. The initial power drift in the first 15 minutes may share causality with the ellipticity drift. This is compatible with a drift in the gain curve, such that the same driving current would result in a different optical output. But again, the injected frequency is still close enough to the center of the gain curve to out-compete other modes. For the duration of this experiment, the laser stays injected and single mode. Except for the momentary loss of injection after 115 minutes, when the power in the main frequency drops by more than 60% for about a second.

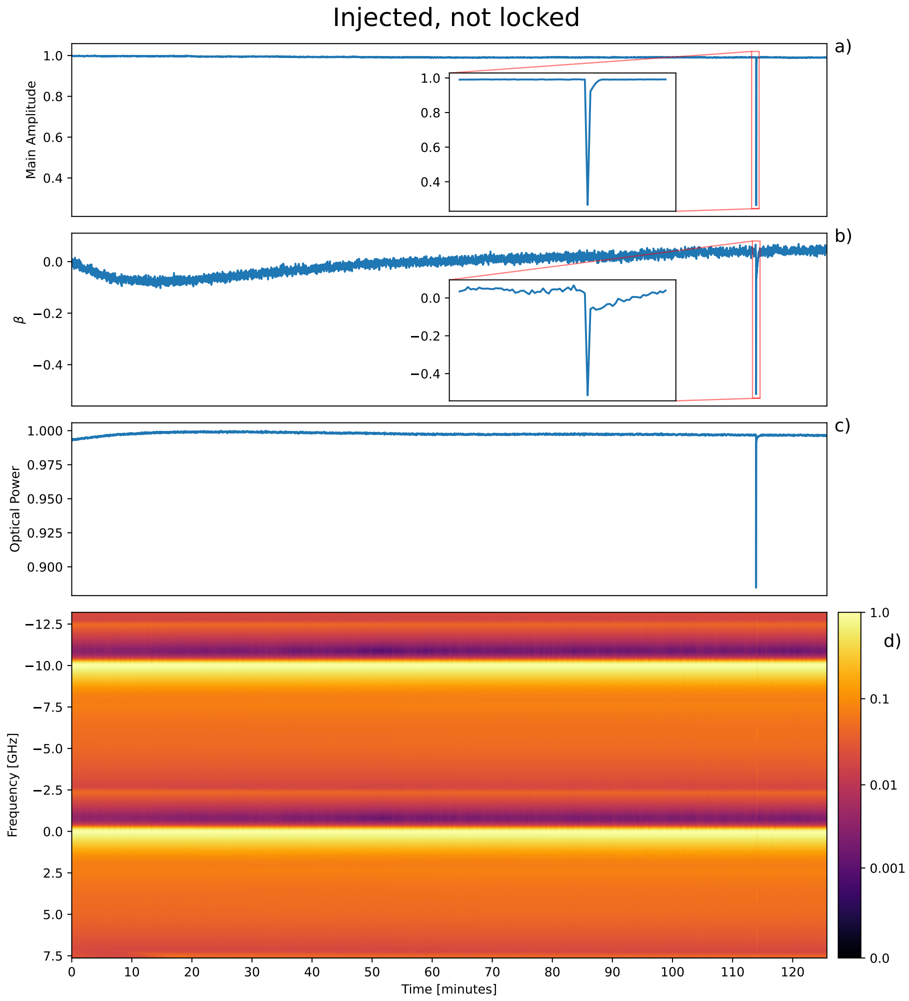

Figure 25: a) Normalized maximum amplitude of the scanning Fabry-Perot, as a function of time. I.e. a measure of the relative amount of optical power in the main frequency. b) Ellipticity as a function of time. c) Normalized optical power as a function of time. d) Logarithmic plot of the spectrum over time. The dominant frequency was meausured by the wavemeter to be $650.50305 \pm 0.0001 Thz$. It is the frequency peak shown here at $[-10, 0] GHz$.

For comparison, the same measurements with active squash locking can be seen in fig. 26. Here, the main amplitude drops off significantly after 11 minutes. This corresponds to the laser developing an additional frequency component at $\pm 3.8 GHz \pm n \cdot 10 GHz$. The diode data sheet states peak wavelength 458 nm. This corresponds to $654 THz$. So this is the most likely frequency of the additional frequency components. This corresponds to $4.0 \cdot 10^2 \pm 10$ FSR distance from the injected frequency. This component carry the majority of the power missing in the injected mode, with amplitudes for this frequency reaching a max of 0.31. Optical power also drops by 2.9% over 110 minutes. In fig. 26c, driving current for the diode is also plotted, since this is the control parameter utilized by the PI system. This plot shows no major correlation between the drop in optical power and the changes to current made by the PI system. However, there are several large steps in the current, probably caused by unidentified perturbations of the system. The ellipticity is maintained throughout, so the PI functionality itself is working as intended.

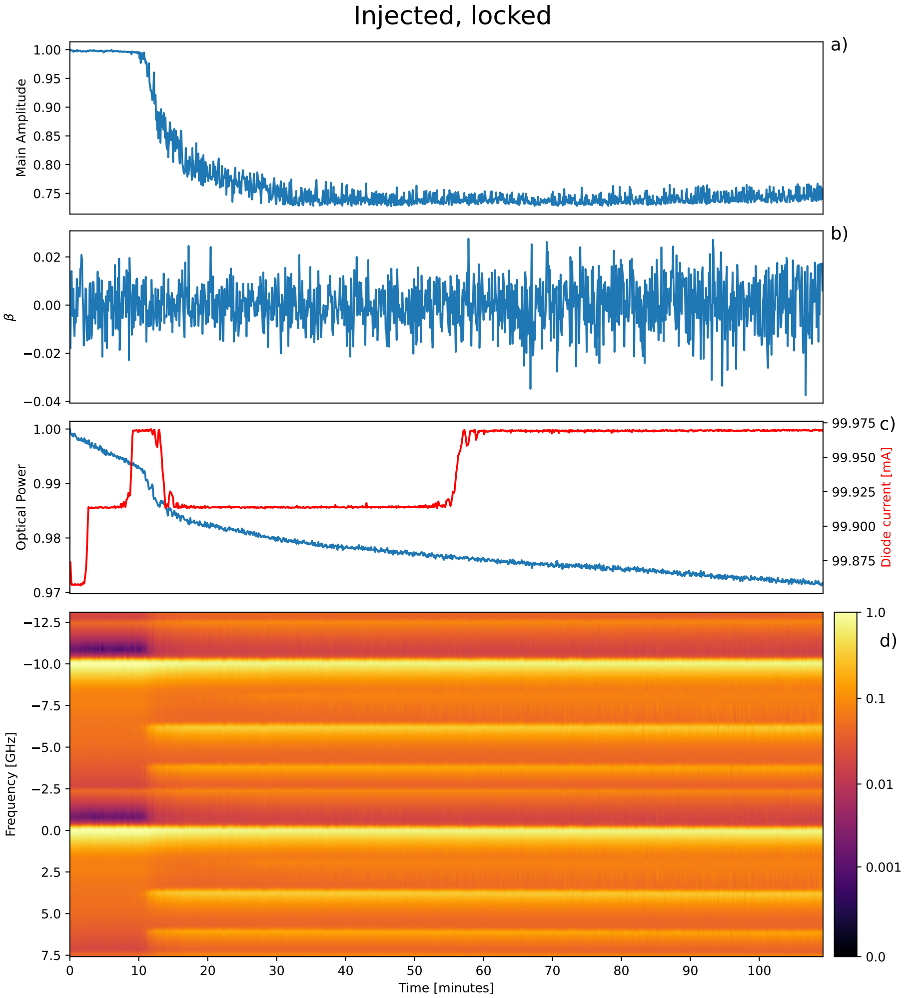

Figure 26: a) Normalized amplitude of the main frequency components, measured by the scanning Fabry-Perot, as a function of time. b) Ellipticity as a function of time. c) Normalized optical power as a function of time in blue. Laser driving current in red. d) Logarithmic plot of the spectrum over time. The dominant frequency was measured by the wavemeter to be $650.50305 \pm 0.0001 Thz$. It is the frequency peak shown here at $[-10, 0] GHz$. After 11 minutes, the spectrum develops a significant extra component at $\pm 3.8 GHz \pm n \cdot 10 GHz$.

3.4.5 Discussion of the squash locking results

The squash locking method for frequency stabilization has been developed in the Hosten group at the Institute for Science and Technology Austria. Their results on the subject are published in two articles [15][22] that are the basis for the squash locking experiments described in this thesis. Their first paper on the subject uses a triangular cavity, external to the diode, to obtain an ellipticity measurement for use as an error signal. This is not comparable to our setup. Their second publication on the subject uses a diode laser, and the cavity used to obtain an ellipticity measurement is simply the internal cavity of the diode. This is the method employed for our measurements. There are a few major differences, though. As a child laser they use a 780nm distributed feedback laser (DFB), with a maximum power of 80mW, injected with 230μW from a reference laser. Our setup uses a 459nm laser, with a maximum of 500mW output, injected with 4mW from a 461nm reference laser. The DFB diode is single frequency, even without injection.

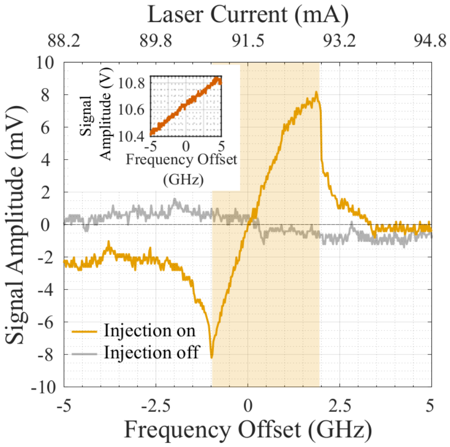

Figure 27: Plot by Mishra, U. et al[22]. Squash locking signal from a 780nm DFB laser, for comparison to the results plotted in fig. 22.

Fig. 27 shows an example of the error signal obtained from their experiments. For comparison, fig. 22 shows our data for a similar current scan over an injection point. However, our blue diode is multi-mode when not injected. Resulting in the ellipticity signal behaving very differently away from the injection point. As such, the results presented in the previous section suggests that either further refinement is needed, or the squash locking method may have more limited utility when used on a diode that is multi-mode, when not injected.

3.5 Camera GUI for fluorescence imaging

In the course of the experimental work described in this thesis, the author also developed a python script[2], including a graphical user interface, to facilitate continuous imaging and fluorescence measurements. The following is a brief description of this script. The camera manufacturer also provides imaging software. However, the Python script implements a few key features that are not available in the manufacturer's software:

1. Time averaging
2. Background removal
3. Fluorescence measurements

However since this script is written in python and the manufacturer's software is written in C++, there are some limitations to the GUI script. With the difference in performance from Python to C++, this is expected. And for the majority of the measurements we are using the camera for, this drawback is outweighed by the ability to do live analysis, rather than taking images in the manufacturer's software and analyzing them separately. The live analysis allows for faster optimization of experimental parameters like optical alignment, magnetic coil current or laser detuning, to maximize atomic flux in the cavity. The data used in section 3.3.4 was taken before this Python script was made and was one of the motivating factors in developing it. It would have allowed for averaging of the atomic fluorescence and obtaining less noisy data. A screenshot of the GUI can be found in appendix B. The image on the right side of the GUI shows a view into the cavity. However, the cavity is not visible, since the background removal feature is activated. So only the atomic fluorescence shows, including weak indirect scattering that partially reveals the shape of the cavity.

---

[2] The script can be found at `https://github.com/Hooverboy/Sr2-Camera`.

4 Summary and outlook

Electromagnetic bias coils were added to the experimental setup and their magnetic field was quantified. With the addition of bias coils, we have shown that the atomic beam can be aligned precisely into the optical cavity used for spectroscopy. An atomic flux of $Q = (2.2 \pm 0.7) \cdot 10^4 s^{-1}$ was measured in the cavity chamber, although this result needs further verification by secondary measurement methods. A transverse atomic beam temperature, perpendicular to the cavity axis, was measured to $T = 2^{+4}_{-1.6} mK$. The data analysis done for temperature measurements also revealed potential atomic lensing.

Squash locking as developed by Fritz Diorico et. al.[15] was explored for use on blue laser diodes. The method was implemented using a digital camera in lieu of an analog quadrature photodetector. Experiments revealed flaws in our implementation, that allowed the injected laser to partially drift in frequency. This reveals difficulties in squash locking diode lasers that are multimode, when not injected.

In the process of acquiring and analyzing data, two Python scripts were developed. One to enable beam shape analysis for use in squash locking, and another to enable live fluorescence measurements.

4.1 Improvements to the atomic beam

The shape of the fluorescence distributions in fig. 15 and fig. 16 are likely determined by a combination of factors. A more thorough experiment could reveal the impact of MOT optical power, laser detuning, and magnetic gradient on the shape of the transverse atomic distribution. For example, different parameters could lead to transverse compression of the most dense parts of the distribution. Meaning higher atomic flux in the cavity could be achieved. The shape of the atomic distributions have not been explained. A framework to model that distribution could also be build. Further, the atomic deflections has only been described in a simplified model. In reality, a continuous MOT can be described more in-depth as an atomic lens, that not only deflects the atomic beam, but also focuses it. This description could be explored, both theoretically and experimentally. Temperature measurements along the cavity axis could also be implemented, as this temperature is of paramount importance for any spectroscopic scheme. Cooling along the cavity axis is planned for the near future.

The imaging software described in section 3.5 already has image averaging implemented. This would allow for much better measurements of atomic deflection. Although with the cavity now installed in the vacuum chamber, the options for laser beam placement, as well as camera placement, are reduced. Precise tuning of the deflection for optimization of atomic flux on the cavity axis could be automated. The Python camera GUI already has options for current control for the bias coils. Other experimental parameters, like laser detuning, could also be controlled in software for fast optimization. At the time of writing, detuning for the optical molasses at the oven nozzle is the same as the MOT detuning. Simply because the MOT laser provides power for the molasses. The laser breadboard used for squash locking experiments is available and is meant to be implemented as a light source for oven nozzle molasses in the near future.

4.2 Improvements to the squash locking method

The laser breadboard that was set up to test squash locking has a few problems. It differs from other laser boards in the lab that have shown greater stability. The parent laser, MOT laser and Zeeman laser, as mentioned in section 3.2 are all able to maintain injection passively for hours, when properly aligned. The laser used in the squash locking experiment would experience mode jumping or loss of injection after a few hours or less. As exemplified in fig. 25 by the injection loss after 115 minutes. One of the possible sources of instability is the diode mount. It was chosen from the sole criterion that it was available. It has previously been discarded for an experiment in the group a few years prior due to bad stability. Although the exact reason has not been quantified. The design of the diode mount also imposed limits on the choice of lens used to collimate the diode. The shorter $f = 4mm$ lenses used in other setups could not be placed close enough to the diode. Instead, a $f = 8mm$ lens was used. This resulted in a larger beam waist, in turn resulting in clipping of the beam on the aperture of the optical isolator. The clipping results in 10% drop in total power. While this is not a critical amount, it is not ideal. Most importantly, this also clips the injecting beam, resulting in suboptimal beam matching between the parent and child laser. This could also be a possible cause of the bad injection stability. As such, a change of diode housing would likely result in better injection stability. Which would be necessary if the laser was to be adapted to actual use in the larger experiment. It would also be worthwhile to run the squash locking experiment again after such adjustments. Or redo the experiment on another laser board to check if the instability of the squash locking method is the result of a flawed implementation or limitations of the hardware. Of particular interest is the fact that the initial paper on squash locking discusses a polarization filtering of the signal to the quadrature photo diode. In their case, it enhances the strength of the error signal. A similar method might benefit our setup.

The Python script that calculates an error signal from a camera image could also be improved. It might be that the error signal could be enhanced by selecting other quadrants of the beam and doing other computations than the simple $\beta = p_1 + p_3 - \epsilon(p_2 + p_4)$. The computation of the best quadrant selection could even be automated by taking a series of images, while scanning diode current over an injection point, and calculating the quadrants that would result in the best error signal.

The Fabry-Perot Resonator used in the squash locking experiments could also be of broader utility in the experiment. With a small, separate optical breadboard, it could monitor several injected laser simultaneously, if optical fibers were run from each laser. The width of the peaks in the trace could likely also be improved drastically with better optical alignment and mode-matching.

References

1. Argus, D. & Heflin, M. Plate Motion and Crustal Deformation Estimated with Geodetic Data from the Global Positioning System. *Geophysical Research Letters* **22,** 1973–1976 (Sept. 1995).
2. Bothwell, T., Kennedy, C. & Aeppli, A. e. a. Resolving the gravitational redshift across a millimetre-scale atomic sample. *Nature* **602,** 420–424 (Feb. 2022).
3. Narayan, R. & Quataert, E. Black holes up close. *Nature* **615,** 597–604 (2023).
4. Hinkley, N. *et al.* An Atomic Clock with 10^{-18} Instability. *Science* **341,** 1215–1218 (Sept. 2013).
5. Wang, Y., Lu, X., Lu, B., Kong, D. & Chang, H. Recent Advances Concerning the 87Sr Optical Lattice Clock at the National Time Service Center. *Applied Sciences* **8.** ISSN: 2076-3417 (2018).
6. Chu, S., Hollberg, L., Bjorkholm, J. E., Cable, A. & Ashkin, A. Three-dimensional viscous confinement and cooling of atoms by resonance radiation pressure. *Phys. Rev. Lett.* **55,** 48–51 (1 July 1985).
7. Chu, S., Bjorkholm, J. E., Ashkin, A. & Cable, A. Experimental Observation of Optically Trapped Atoms. *Phys. Rev. Lett.* **57,** 314–317 (3 July 1986).
8. Phillips, W. D. & Metcalf, H. Laser Deceleration of an Atomic Beam. *Phys. Rev. Lett.* **48,** 596–599 (9 Mar. 1982).
9. Metcalf, H. & Van der Straten, P. *Laser Cooling and Trapping* ISBN: 9780387987477 (Springer, 1999).
10. Griffiths, D. J. & Schroeter, D. F. *Introduction to Quantum Mechanics* 3rd ed. (Cambridge University Press, 2018).
11. Foot, C. *Atomic Physics* ISBN: 9780198506959 (OUP Oxford, 2005).
12. Hadley, G. Injection locking of diode lasers. *IEEE Journal of Quantum Electronics* **22,** 419–426 (1986).
13. Coldren, L., Corzine, S. & Mashanovitch, M. *Diode Lasers and Photonic Integrated Circuits* ISBN: 9780470484128 (Wiley, 2012).
14. Ohtsubo, J. *Semiconductor Lasers: Stability, Instability and Chaos* 4th ed. ISBN: 978-3-319-56137-0 (Springer International Publishing, 2017).

15. Diorico, F., Zhutov, A. & Hosten, O. *Laser-cavity locking at the* 10^{-7} *instability scale utilizing beam elipticity* 2022. arXiv: `2203.04550 [physics.optics]`.

16. Ye, J., Ma, L.-S. & Hall, J. L. Ultrasensitive detections in atomic and molecular physics: demonstration in molecular overtone spectroscopy. *J. Opt. Soc. Am. B* **15,** 6–15 (Jan. 1998).

17. Christensen, B. T. R. *Laser Stabilization With Laser Cooled Strontium* PhD thesis (University of Copenhagen, Apr. 2016).

18. Griffiths, D. *Introduction to Electrodynamics* 3rd ed. ISBN: 9781108420419 (Cambridge University Press, 2017).

19. Restrepo, A., Franco, E., Cadavid, H. & Pinedo, C. A simple geomagnetic field compensation system for uniform magnetic field applications. *Revista Facultad de Ingeniería* **2017,** 65–71 (June 2017).

20. Osmundsen, J. H. & Gade, N. Influence of optical feedback on laser frequency spectrum and threshold conditions. *IEEE Journal of Quantum Electronics* **19,** 465–469 (1983).

21. Patil, D. *Semiconductor Laser Diode: Technology and Applications* ISBN: 9789535105497 (IntechOpen, 2012).

22. Mishra, U. *et al. Monitoring and active stabilization of laser injection locking using beam ellipticity* 2022. arXiv: `2212.01266 [physics.optics]`.

A Squash locking GUI

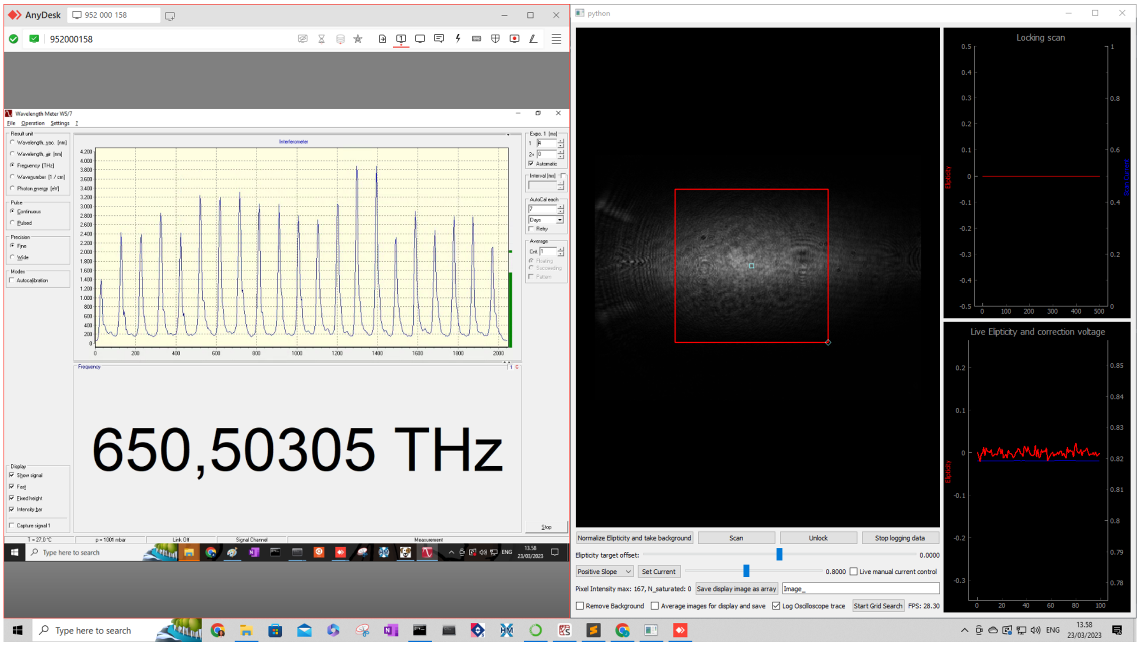

650,50305 THz

Elipticity target offset: 0.0000

0.8000 ☐ Live manual current control

Pixel Intensity max: 167, N_saturated: 0

Image_

☐ Remove Background ☐ Average images for display and save ☑ Log Oscilloscope trace

FPS: 28.30

13.58 23/03/2023

Figure 28: Screenshot from using the squash locking GUI. Left side of screen is the output of the high finesse wavemeter. Right side of the screen is the Python GUI controlling the squash locking and logging of experimental data from the camera and the oscilloscope for the scanning Fabry-Perot.

B Imaging GUI

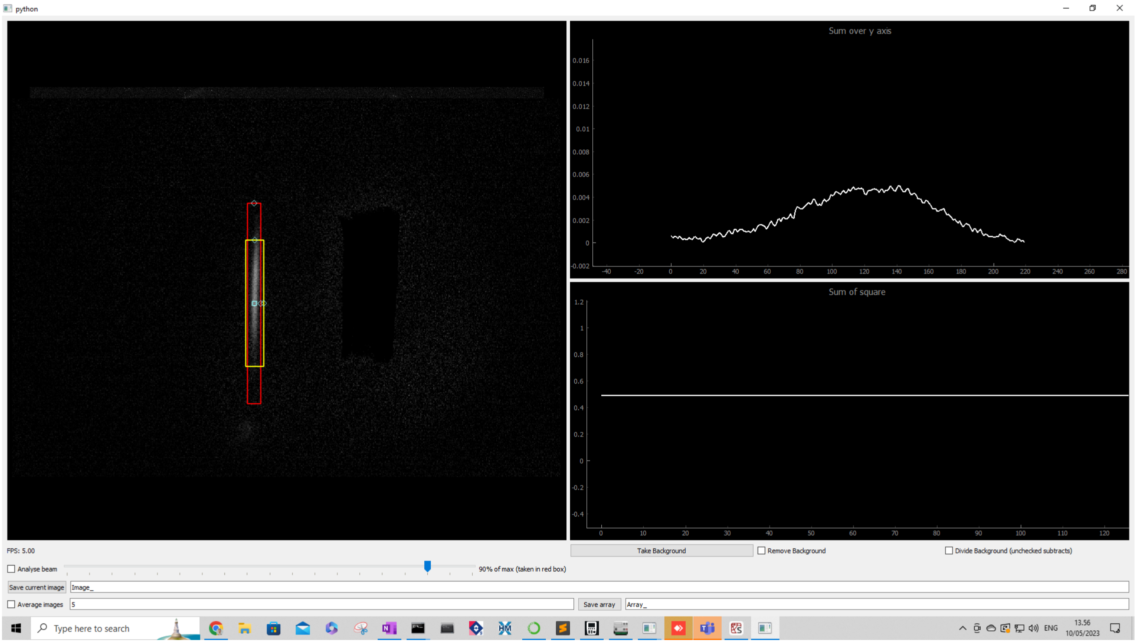

FPS: 5.00

90% of max (taken in red box)

Save current image: Image_

Average images: 5

Save array: Array_

Figure 29: Screenshot from using the fluorescence GUI. Left window is the live camera image. Top right plot is the fluorescence in the red box, summed vertically. Bottom right plot is a rescaled fluorescence in the yellow box, summed in both axis.